JGR Space Physics

RESEARCH ARTICLE
10.1029/2022JA030753

Electron Heat Fluxes Generated by Intense Whistler Waves at the Upper Ionospheric Altitudes

George V. Khazanov[1], Qianli Ma[2,3], and Mike Chu[4]

[1]NASA Goddard Space Flight Center, Greenbelt, MD, USA, [2]Center for Space Physics, Boston University, Boston, MA, USA, [3]Department of Atmospheric and Oceanic Sciences, University of California, Los Angeles, CA, USA, [4]The Space Weather Lab, George Mason University, Fairfax, VA, USA

Key Points:

- Magnetospheric hiss and chorus waves is an implicit heat source of the cold electrons in ionosphere and magnetosphere
- SuperThermal Electron Transport simulations show the electron heat flux formation due to whistler waves through magnetosphere-ionosphere energy interplay
- Our model evaluates the elevated upper ionospheric electron temperature driven by strong whistler waves in magnetosphere

Correspondence to:

G. V. Khazanov,
George.V.Khazanov@nasa.gov

Citation:

Khazanov, G. V., Ma, Q., & Chu, M. (2022). Electron heat fluxes generated by intense whistler waves at the upper ionospheric altitudes. *Journal of Geophysical Research: Space Physics*, *127*, e2022JA030753. https://doi.org/10.1029/2022JA030753

Received 16 JUN 2022
Accepted 23 AUG 2022

Author Contributions:

Data curation: Qianli Ma
Supervision: Mike Chu
Visualization: Qianli Ma
Writing – original draft: Qianli Ma

Abstract Magnetospheric whistler waves, chorus and hiss, can't provide the resonance heating of the core electron plasma population. However, these whistler-mode branches, can *implicitly* participate in the heating processes of the core plasma thermal electron population by triggering the electron precipitation over a broad energy range from the magnetosphere and subsequent atmospheric ionization processes leading to the production of superthermal electron population. These superthermal electrons play a large role in the magnetosphere-ionosphere-atmosphere energy interplay with participation of both magnetically conjugate hemispheres, and their Coulomb interaction with background magnetospheric thermal electrons. Using strong hiss and chorus wave events measured by the Van Allen Probes and SuperThermal Electron Transport code, we evaluate the formation of electron heat fluxes at the upper ionospheric altitudes and discuss their consequences on the formation of electron temperature. It is found that chorus and hiss waves that initiate the precipitation of magnetospheric electrons with energies below 30 keV and the follow-up production of secondary electrons play an important role in the energy balance of ionosphere-magnetosphere system.

Plain Language Summary Electron heat flux that comes from the magnetosphere to the upper ionospheric altitudes controls the value of electron temperature in the core plasma, and, as a result, the total electron density content that is required for different kinds of space weather applications. This paper offers the new mechanism of electron heat flux formation that is based on wave-particle interaction processes that include whistler waves: hiss and chorus. These waves can't directly heat the cold magnetospheric electrons. They, however, resonate with high energy magnetospheric electrons initiating precipitation into the atmospheres of magnetically conjugate regions and, as result, their multiple passes between the northern and southern hemispheres. High energy electron interactions with the ionospheric neutral populations lead to the production of the secondary electrons escaping back to the magnetospheric altitudes where they become trapped and move between the points of reflection. These electrons, as well as degraded primary precipitated electrons, interact with the core cold magnetospheric electrons continuously losing their energy via Coulomb collisional processes and form the electron heat flux that defines electron temperature at upper ionospheric altitudes. The newly suggested mechanism plays a very important role in the energy balance of ionosphere-magnetosphere system and must be considered in the ionospheric space weather simulations.

1. Introduction

Whistler-mode waves, chorus and hiss, play a very important role in radiation belt dynamics influencing 10 keV–1 MeV electron energies (Thorne, 2010). This was recognized and widely discussed by many authors considering different aspects of radiation belt physics (e.g., Baker et al., 2014; Horne & Thorne, 1998; Lyons & Thorne, 1973; Meredith, Horne, Glauert, et al., 2006; Meredith et al., 2007; Ni et al., 2013, 2014; Thorne et al., 2010). Only recently it also was recognized that hiss waves can influence much lower (compared to radiation belt electrons) energies from tens of eV to 1 keV via Landau resonance process (J. Li et al., 2019). Heating of superthermal electron (SE) population in the tens eV energy range and follow up Coulomb collisions of these electrons with surrounding cold electrons, make hiss waves also important for energy deposition processes to the core magnetospheric and ionospheric thermal electron energies below 1–2 eVs. One of the issues for these SE acceleration processes is the requirement of a seed SE population below the energy of 500 eV (Khazanov & Ma, 2021; J. Li et al., 2019).

As we proceed with presenting results of this paper, it will be demonstrated (Section 2) that magnetospheric whistler waves, chorus and hiss, usually can't provide the resonance heating of the core electron plasma population, as, for example, oblique electromagnetic ion cyclotron (EMIC) waves do via Landau resonance process (Khazanov, 2010). Both chorus and hiss waves, however, can *implicitly* participate in the heating process of the core plasma thermal electron population by triggering the broad energy range of the electron precipitation from the magnetosphere and follow-up atmospheric ionization processes, production of SE population, and their magnetosphere-ionosphere-atmosphere (MIA) energy interplay with participation of both magnetically conjugate hemispheres. This idea of the *implicit heating* was proposed by Khazanov et al. (2017, 2020) who used relatively low intensity of chorus and electron cyclotron harmonics (ECH) waves with magnitudes of 10 pT and 1 mV/m, respectively. The previous analysis was performed without any specific spacecraft data and used simplified assumptions of Gaussian function to represent the wave energy distribution with frequency for both wave modes.

In this manuscript we continue to develop this idea of *implicit heating* of thermal electron population by magnetospheric whistlers, using strong hiss and chorus waves measured by the Van Allen Probes. We selected three hiss wave events at the dayside in the plasmaspheric plumes at $L > 5.5$, where the electron precipitation driven by hiss is the most intense based on the previous survey (Ma et al., 2021). The three chorus wave events are selected at the nightside in the plasma trough region during disturbed conditions with high auroral electrojet (AE) activity.

This paper is organized into the following sections. Section 2 describes whistler-mode wave resonances that drive SE precipitations. The Van Allen Probes observations we used in this study are presented in Section 3. The simulation scenario of calculating electron heat fluxes driven by wave-particle interaction (WPI) processes is presented in Section 4. The results of hiss and chorus wave-driven SE precipitation and electron heat fluxes are discussed in Section 5, in connection with SuperThermal Electron Transport (STET) based methodology of heat flux calculation presented in the Appendix A of this manuscript. Finally, in Sections 6 and 7, we present the qualitative and quantitative analysis of electron heat flux formation and discuss and summarize their consequences for the electron temperature formation and MIA energy interchange in space plasma.

2. Whistler Waves Resonances

Whistler-mode chorus and hiss waves are right-hand-polarized electromagnetic waves which can cause electron pitch angle scattering and acceleration in the Earth's magnetosphere through multiple harmonic resonances (Horne & Thorne, 1998; Thorne, 2010; Thorne et al., 2021). The chorus waves are mainly observed at frequencies from the lower hybrid resonance frequency (f_{LHR}) to the electron gyrofrequency (f_{ce}) and categorized as the lower-band (LBC) and upper-band (UBC) chorus by the frequency separation at $0.5f_{ce}$ (W. Li et al., 2009; Meredith et al., 2020). The Van Allen Probes statistics (W. Li et al., 2016) revealed two major propagation components of chorus, including a group of quasi-field-aligned waves with large magnetic field intensities, and a group of oblique waves propagating at normal angles between Gendrin angle and the resonance cone angle. The hiss waves (W. Li et al., 2015; Meredith et al., 2018) are mainly observed at frequencies from 20 to 4,000 Hz and below $0.5f_{ce}$. The hiss waves usually propagate close the field-aligned direction in the plasmaspheric plumes and outer plasmasphere (W. Li et al., 2019; Shi et al., 2019). As the waves propagate, the wave normal angles become larger at higher latitudes or deeper inside the plasmasphere (Bortnik et al., 2011).

The electron resonance energy depends on wave frequency and normal angle. Figure 1 presents the resonance energies calculated over the typical frequencies and using different total electron densities for whistler-mode hiss and chorus waves. To estimate the contribution to electron precipitation, the resonance energy is evaluated for the electrons with 0° pitch-angle. The cold plasma dispersion relation is used in the calculations. The magnetosonic waves have wave normal angles close to 90° (Ma et al., 2013) and are not included in Figure 1.

The electron minimum resonance energy due to chorus (Figure 1a) is higher than 1 keV except for the waves with frequencies higher than $\sim 0.7f_{ce}$ or the wave normal angles close to the resonance cone. However, the wave dispersion relation needs to be corrected by hot plasma effects for the chorus waves with normal angles close to the resonance cone (Ma et al., 2017). Chorus waves could also heat the several hundred eV electrons at small pitch-angles through Landau resonance (Figure 1b).

Hiss waves cause the electron scattering mostly at energies above several keV through gyroresonance (Figure 1c). The resonance energy increases to above 10 keV for the wave frequencies below 500 Hz. The Landau resonance

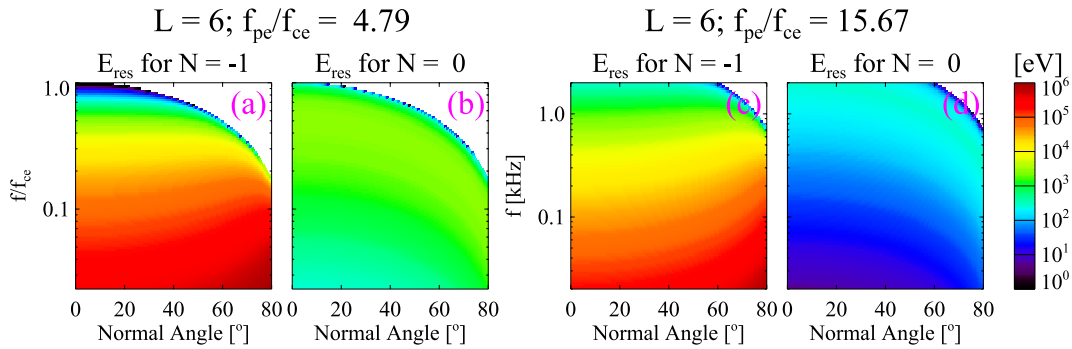

Figure 1. Resonance energies of electrons with 0° pitch angle due to whistler-mode waves at $L = 6$, considering the fundamental gyroresonance ($N = -1$) and Landau resonance ($N = 0$). (a, b) Resonance energy as a function of wave normal angle and wave frequency calculated using the plasma trough electron density from Sheeley et al. (2001) for wave frequencies from the lower hybrid resonance frequency ($f/f_{ce} \sim 0.02$ for 100% proton composition) to the electron gyrofrequency (f_{ce}), which is representative for chorus waves. (c, d) Resonance energy calculated using the plasmasphere electron density from Sheeley et al. (2001) for wave frequencies from 20 Hz to 2 kHz (~0.5 f_{ce}), which is representative for hiss waves. The ratios between plasma frequency f_{pe} and f_{ce} are 4.79 and 15.67 for chorus and hiss, respectively.

energy of hiss waves (Figure 1d) is generally lower than the cyclotron resonance energy of the electron resonance energy due to chorus. The Landau resonance energy of hiss decreases from hundreds of eV to tens of eV with decreasing wave frequency. Therefore, hiss waves may cause precipitation through pitch-angle scattering at energies above several keV, and field-aligned electron acceleration from tens to hundreds of eV through Landau resonance.

3. Van Allen Probes Observations

Whistler-mode chorus waves are generated by the energetic electrons with anisotropic pitch-angle distributions in the plasma trough (Fu et al., 2014; W. Li et al., 2010). During intense geomagnetic storms, the plasmapause is eroded to low L shells, and the electron injection activity provides the source energy for chorus wave generation, leading to the high occurrence rate of chorus over the nightside-dawn-dayside sectors outside the plasmapause (Agapitov et al., 2013; Meredith et al., 2012, 2014). The average wave amplitude reaches values higher than 100 pT during the condition AE > 300 nT (Meredith et al., 2020), with the highest average wave intensity observed near dawn sector at low magnetic latitudes. The LBC wave amplitude is on average higher than UBC wave amplitude.

The hiss waves in the plasmasphere and plumes mainly originate from the wave propagation by chorus waves at high L shells (Bortnik et al., 2008, 2009; Chen, Bortnik, et al., 2012), the lightning-generated whistlers from the Earth's ionosphere (Bortnik et al., 2003; Meredith, Horne, Clilverd, et al., 2006; Sonwalkar & Inan, 1989), and wave amplification by the energetic electron injections at the outer edge of the plasmasphere (Chen, Li, et al., 2012; Chen et al., 2014; W. Li et al., 2013). The average wave amplitude of hiss is higher than 100 pT at the dayside over $2 < L < 6$ during the disturbed condition AL* < −500 nT, where AL* is the minimum AL index in the previous 3 hr (W. Li et al., 2015). The frequency of peak wave intensity is ~100–300 Hz and decreases with increasing L shell. Strong hiss waves with field-aligned propagation are observed in the plasmaspheric plumes where the electron injections may provide the local wave amplification (W. Li et al., 2019).

In this study, we use the Van Allen Probes (Mauk et al., 2013) observation of the waves and electrons in the Earth's inner magnetosphere. The total electron density is inferred from the upper hybrid resonance frequency line measured by the High Frequency Receiver (HFR) of Electric and Magnetic Field Instrument Suite and Integrated Science (EMFISIS) instrument (Kletzing et al., 2013; Kurth et al., 2015). The wave magnetic power spectrogram is obtained using the three component wave measurements by Waveform Receiver (WFR). The total magnetic field is measured by the magnetometer at 1 s cadence derived on ground from the 64 samples/s measurements. The Energetic Particle, Composition, and Thermal Plasma (ECT) suite provides the particle measurements over a broad energy range and full pitch-angle coverage (Spence et al., 2013). We use the Helium, Oxygen, Proton, and Electron (HOPE; Funsten et al., 2013) Mass Spectrometer measurements to obtain the electron flux at different pitch-angles and 15 eV–50 keV energies. During our selected events, the electron flux

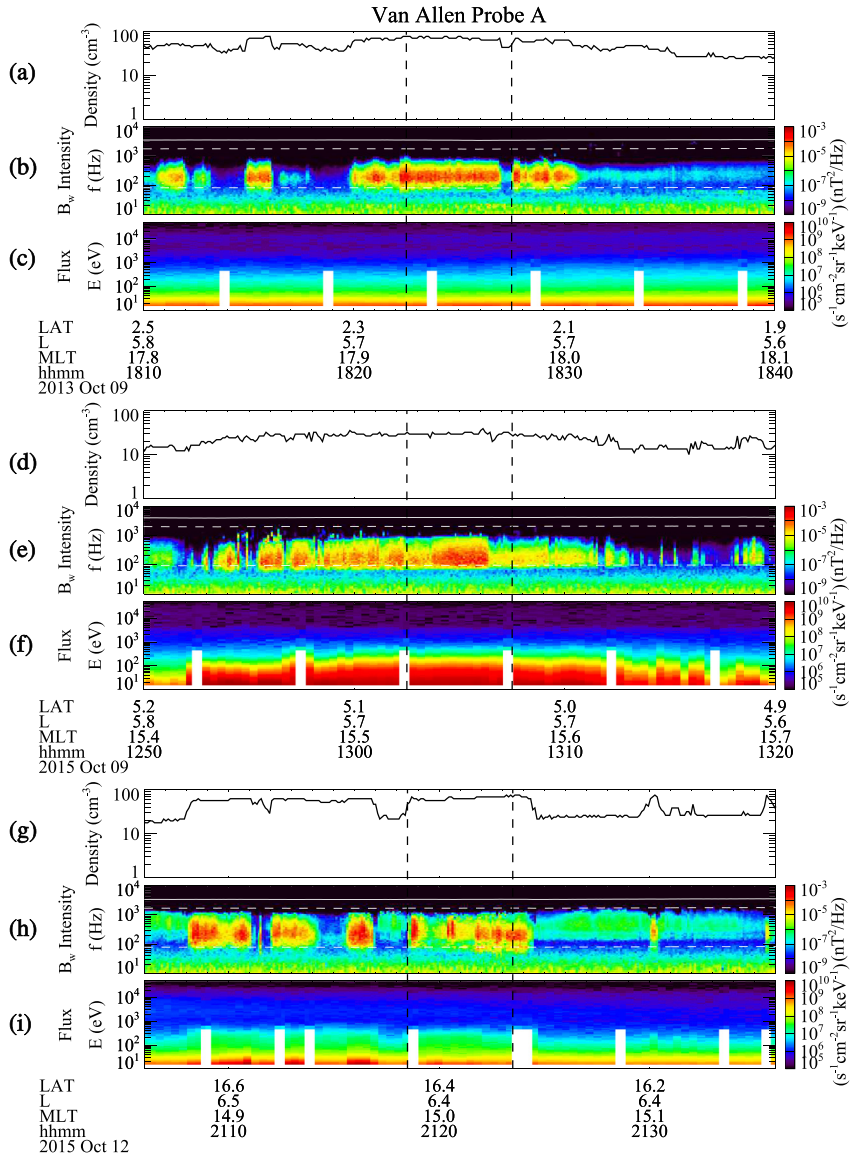

Figure 2. Van Allen Probe A observation of the hiss and electrons during 30-min intervals on (a–c) 09 October 2013, (d–f) 09 October 2015, and (g–i) 12 October 2015. (a, d, and g) Total electron density inferred from the upper hybrid resonance frequency line measured by High Frequency Receiver; (b, e, and h) magnetic power spectrogram measured by Waveform Receiver, where the three white lines are f_{ce}, 0.5 f_{ce}, and f_{LHR} at the magnetic equator, respectively; (c, f, and i) energy spectrogram of electron flux at 15 eV–50 keV energies measured by Helium, Oxygen, Proton, and Electron. The two black dashed lines indicate the interval used for electron precipitation analysis during each hiss wave event.

measurements are not affected by the spacecraft generated photoelectrons since the flux at the lowest energy channel is not anti-correlated with the density (Scudder et al., 2000).

3.1. Hiss Wave Events

Figure 2 shows the three hiss wave events observed by Van Allen Probe A in the plasmaspheric plumes. All three events are observed during the recovery phase of geomagnetic storms, with intense substorm activity suggested by the large AE index a few hours before the event (not shown). The hiss waves were observed near the spacecraft apogee over the afternoon MLT sector at L shells of 5.7, 5.7, and 6.4, but different magnetic latitudes of ∼2.2°, 5°, and 16.4°. The hiss waves were mainly observed at frequencies from 50 Hz to $f_{ce}/2$. The hiss wave intensities were modulated by the total electron density structures, showing strong wave intensification (∼10^{-3} nT^2/Hz) at the

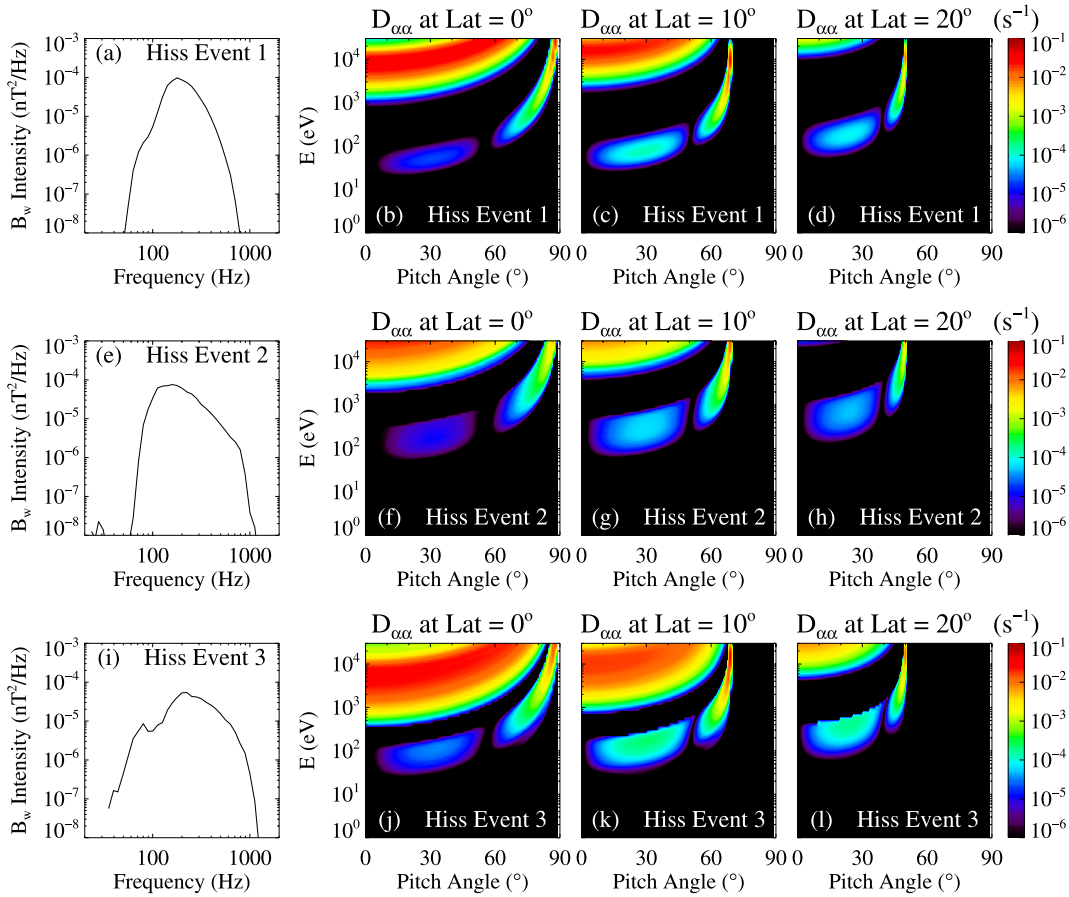

Figure 3. Calculation of local diffusion coefficients for the three hiss wave events. (a, e, and i) The observed frequency spectrum of hiss magnetic power intensity, (b, f, and j) the local pitch-angle diffusion coefficient as a function of electron energy and pitch-angle at 0° magnetic latitude, (c, g, and k) 10° magnetic latitude, and (d, h, and l) 20° magnetic latitude.

relatively high-density region. The absolute values of spacecraft potential were below 5 V during all three events. The electron fluxes at 15 eV–50 keV energies were stable during the first event (Figure 2c). Strong enhancements of electron fluxes at energies below 300 eV were observed during the second hiss wave event, reaching the level of $\sim 10^{10}$ s^{-1} cm^{-2} sr^{-1} keV^{-1} at ~15 eV energy (Figure 2f). During the third event, the electron fluxes at energies below 300 eV were modulated with the total electron density structures (Figure 2i), although the modulation was not as clear as the modulation of hiss waves.

We select 5-min intervals during each hiss wave event to perform the electron precipitation analysis, as shown between the two black dashed lines in Figure 2. The 5-min average wave frequency spectra are shown in Figures 3a, 3e and 3i. During the three events, the average total electron densities are 70, 29, and 63 cm^{-3}, the equatorial electron cyclotron frequencies are 3.5, 4.1 and 3.4 kHz, and the average hiss wave amplitudes are 121, 125, and 124 pT, respectively. With these parameters and the observed wave frequency spectra as inputs, we use the quasilinear model of electron precipitation (Ma et al., 2021) to calculate the local pitch-angle diffusion coefficients at different magnetic latitudes as shown in Figure 3. The wave magnetic power is assumed to be proportional to $\exp\left(-\left(\frac{\tan\theta-\tan\theta_m}{\tan\theta_w}\right)^2\right)$ (e.g., Ni et al., 2013), where θ is the wave normal angle, $\theta_m = 0°$, $\theta_w = 30°$, and the lower and upper cutoffs are at 0° and 45°, respectively. The wave normal angle distributions from EMFISIS Level-4 data product are mainly quasi-field aligned for the plume hiss waves.

The comparison of local diffusion coefficients at different latitudes (Figures 3b–3d, 3f–3h, or 3j–3l) suggests that the electron scattering at energies below 30 keV are mainly due to the hiss waves at latitudes below 20°. The previous studies (Ni et al., 2013; Thorne et al., 2013) modeled plasmaspheric hiss wave normal angle variation as changing from quasi-parallel at equator to oblique at ~40° latitude. For simplicity, we evaluate the electron

scattering effects at energies below 30 keV using the same quasi-parallel wave normal angle distribution at latitudes below 20°. The wave magnetic power is assumed to be the same from the equator to 20° latitude. The simulation results at energies below 30 keV are not sensitive to the wave normal angle assumptions at high latitudes.

Although the observed hiss wave amplitudes were similar among the three events, the electron diffusion coefficients have different distributions due to difference in resonance energy. During hiss event 1 on 09 October 2013, the hiss waves cause pitch-angle scattering at energies above ~1 keV at the equator, and Landau resonance acceleration of electrons from tens of eV at small pitch-angles to above 1 keV at large pitch-angles (Figure 3b). At higher latitudes, the hiss waves could scatter or accelerate electrons at higher energies or lower pitch-angles (Figures 3c and 3d). During hiss event 2 on 09 October 2015 (Figures 3f–3h), the electrons at higher energies are scattered by hiss waves compared to the scattering during event 1. The higher resonance energy is due to the lower total electron density and lower wave frequency of peak wave intensity in event 2 compared to those in event 1. During hiss event 3 on 12 October 2015 (Figures 3j–3l), the pitch-angle scattering of electrons is extended to several hundred eV energies, because the hiss wave power is extended to higher frequencies during event 3 than that during event 1. Therefore, it is important to incorporate the observed wave frequency spectrum in the modeling, in order to accurately quantify the electron precipitation during each event. For the electron precipitation at energies below 30 keV, the hiss waves during event 3 may be the most effective. However, we also note that the electron fluxes at 15–300 eV energies during event 2 (Figure 2f) are significantly larger than the fluxes during other two events. The detailed comparison among the three events on the formation of electron heat flux requires further STET modeling by considering the coupling of magnetosphere and ionosphere processes.

3.2. Chorus Wave Events

Figure 4 presents the three chorus wave events observed by the Van Allen Probe A at the nightside outside the plasmapause. Chorus event 1 (01 March 2013) was observed during the main phase of a modest geomagnetic storm and events 2 (03 February 2015) and 3 (08 May 2018) were observed during the recovery phase. All three events were observed with the highest AE index in the previous 1 hr larger than 500 nT, suggesting nightside electron injections. During chorus event 1 (Figure 4b), the major power of chorus was at frequencies below $0.5f_{ce}$ reaching large intensities of $\sim 10^{-3}$ nT^2/Hz, while the UBC waves were weak. During chorus event 2 (Figure 4e), both UBC and LBC were observed in frequency bands separated by $0.5f_{ce}$ frequency. Each band of chorus had relatively narrow frequency range and was more stable in time compared to that in event 1. During the chorus event 3 (Figure 4h), the LBC frequency spectrogram shows two frequency bands, while the UBC was not observed. The intensity of lower frequency band was higher than the higher frequency band intensity. In addition, there were several strong wave intensifications ($\sim 10^{-3}$ nT^2/Hz) lasting for a few seconds each, at frequencies between the two bands of chorus. The electron fluxes at 15 eV–50 keV energies observed during event 1 were higher than the fluxes observed during events 2 and 3 (Figures 4c, 4f and 4i), possibly related to the geomagnetic storm activity.

We select the 5-min intervals during the three chorus wave events to analyze the electron precipitation as marked by the black dashed lines in Figure 4. Figures 5a, 5e and 5i show the chorus wave frequency spectra as a function of normalized wave frequency during the three events. The average total electron densities are 2.6, 1.9, and 1.2 cm^{-3}, the equatorial electron frequencies are 2.1, 3.2, and 3.2 kHz, and the average chorus wave amplitudes are 271, 109, and 146 pT, respectively. Using the quasilinear modeling of electron precipitation (Ma et al., 2020), we calculate the local pitch-angle diffusion coefficients as shown in Figure 5. The LBC and UBC waves are assumed to have a latitude range from equator to 20° and from equator to 10°, respectively. For simplicity, the same quasi-parallel propagating wave normal angle distribution ($\theta_m = 0°$, $\theta_w = 30°$, lower cutoff at 0° and upper cutoff at 45°) is used for chorus waves and hiss waves in the plumes. The latitude distribution and wave normal angle distribution of chorus are similar to the distributions in Ni et al. (2011).

The pitch-angle scattering rates are significantly different for the three chorus wave events. During chorus event 1 (Figures 5b–5d), the local diffusion coefficient reaches higher than 0.1 s^{-1} at several keV energies near the equator, and the scattering extends to tens of keV energies with lower efficiency, due to the weak waves at the high frequencies. Similar to the results of hiss waves, the electrons at energies below 30 keV are most scattered by the chorus waves at low latitudes. During chorus event 2 (Figures 5f–5h), the UBC and LBC waves cause the electron scattering at energies below and above ~5 keV, respectively. The UBC during event 2 causes faster electron scattering loss at ~300 eV–2 keV energies than the chorus during event 1, although the scattering during

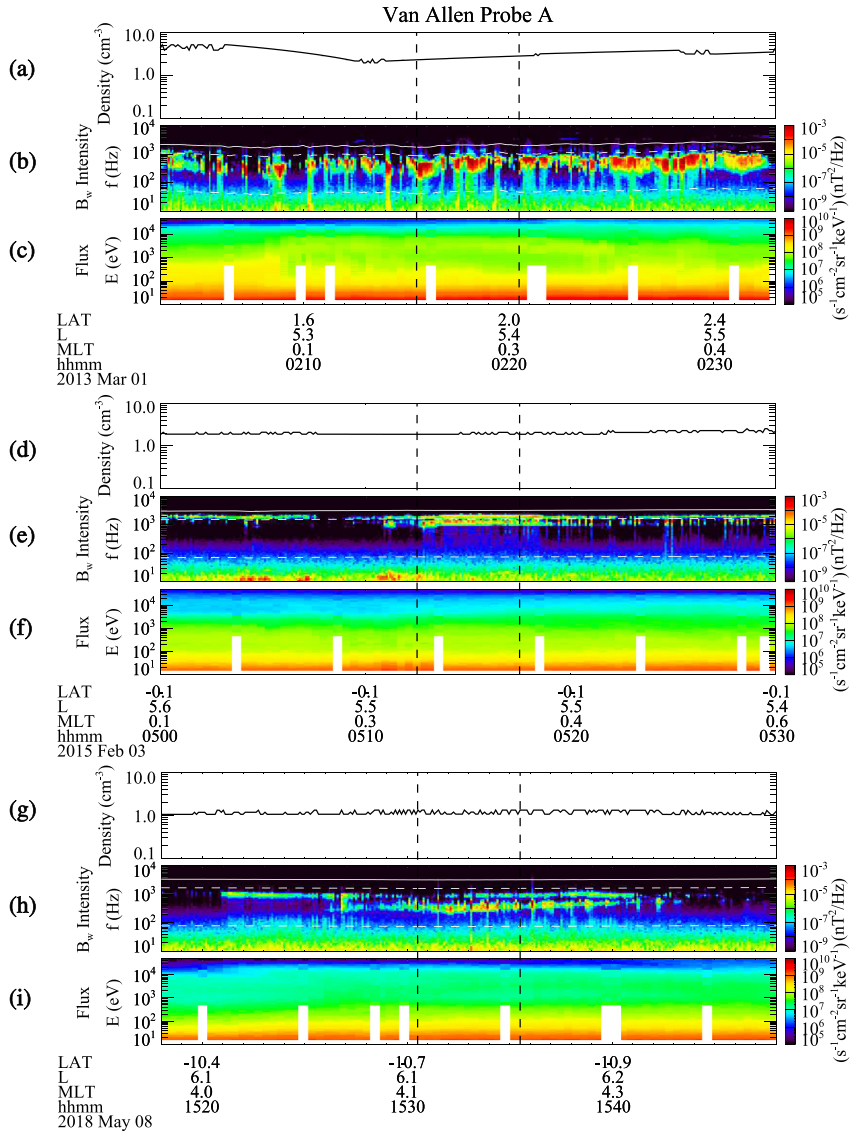

Figure 4. Same format as Figure 2 but for the Van Allen Probes observation during three chorus wave events.

event 1 is overall faster at other energies. During chorus event 3 (Figures 5j–5l), the electron energy of pitch-angle scattering is overall higher than 30 keV, and only the effect of Landau resonance is evident at energies above 2 keV. The chorus wave frequency is lowest during event 3, corresponding to the high resonance energy of electrons. Therefore, the chorus waves with relatively high frequencies ($f > \sim 0.2 f_{ce}$) are important for the pitch-angle scattering loss of electrons at energies below 30 keV which originate from the plasma sheet.

4. Simulation Scenarios

4.1. Overall Picture

As discussed by Khazanov et al. (2020), depending on the latitudinal location, the electron heat flux can be formed by different magnetospheric processes. Among them are collisional heating of the thermal electrons by ring current protons (Cole, 1965); Landau damping of ion cyclotron waves on the magnetospheric thermal electrons (Cornwall et al., 1971); the damping of kinetic Alfven waves (Hasegawa & Mima, 1978); ring current O^+ ions driving thermal electron heating and formation of Stable Auroral Red (SAR) arcs (Kozyra et al., 1987). Khazanov et al. (2007) considered both ring current Coulomb collisions and EMIC waves contribution to the

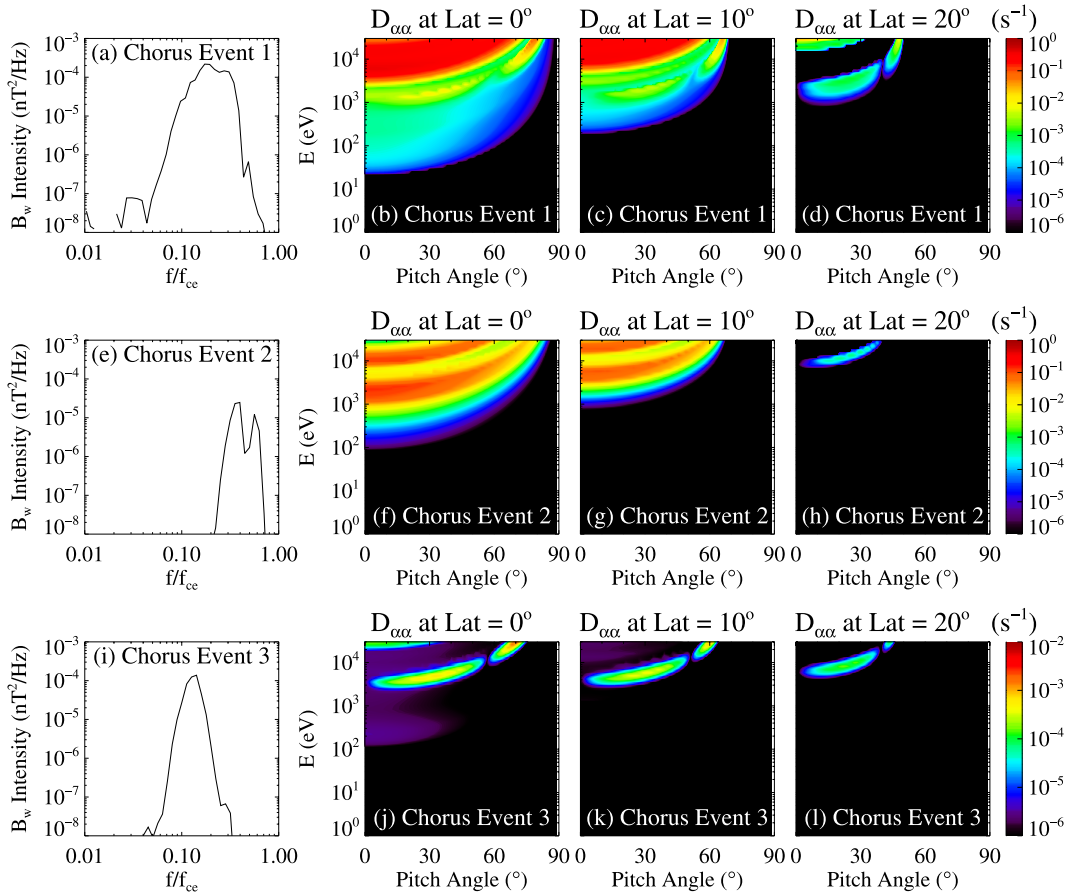

Figure 5. Same format as Figure 3 but for the diffusion coefficients during three chorus wave events.

formation of the thermal electron fluxes that are self-consistently calculated for the specific magnetospheric storm conditions.

In the example of Van Allen Probes observations as presented in Section 3, the major source of the electron heat fluxes are coming from the superthermal electron (SE) fluxes of ionospheric origin in the energy range of 1–500 eV: photoelectrons and secondary electrons. Photoelectrons are produced on the dayside via interaction of solar UV and X-Ray radiations with the neutral atmosphere. The secondary electrons result from the interaction of high energy electrons of magnetospheric origin at >1 keV energies, with the neutral particles. These SE deposit their energy to the thermal electrons via elastic Coulomb collisions which are then conducted down to the ionosphere as a thermal heat flux. Detailed analysis of the production processes of SE are discussed by Schunk and Nagy (2009) and Khazanov (2010). This manuscript focuses on the high energy electron precipitation driven by strong whistler waves and its affiliated energy interplay with photo-, secondary and thermal electron populations. We refer the readers to Khazanov (2010) that provides detailed analysis of electron heat flux formation via ionospheric photoelectrons.

The formation of electron thermal fluxes via electron precipitation dynamics driven by hiss and chorus waves with participation of ionospheric photoelectrons is shown in Figure 6 (purple arrow). In this area the wave–particle interactions (WPI) drive electron precipitation (Primary Flux as shown in Figure 6) and create the secondary-electron fluxes that escape to the magnetosphere where they deliver their energy via Coulomb collisional processes to the thermal electrons (see Khazanov et al. (2020) for details). Depending on the atmospheric solar zenith angle values in the magnetically conjugate regions, photoelectrons also actively participate in the formation of electron heat fluxes that are coming from the magnetosphere to ionosphere and support electron temperature (Te) formation. These above two electron thermal flux sources would be further discussed and elaborated in Section 5 of this paper with the reference to Figure 6.

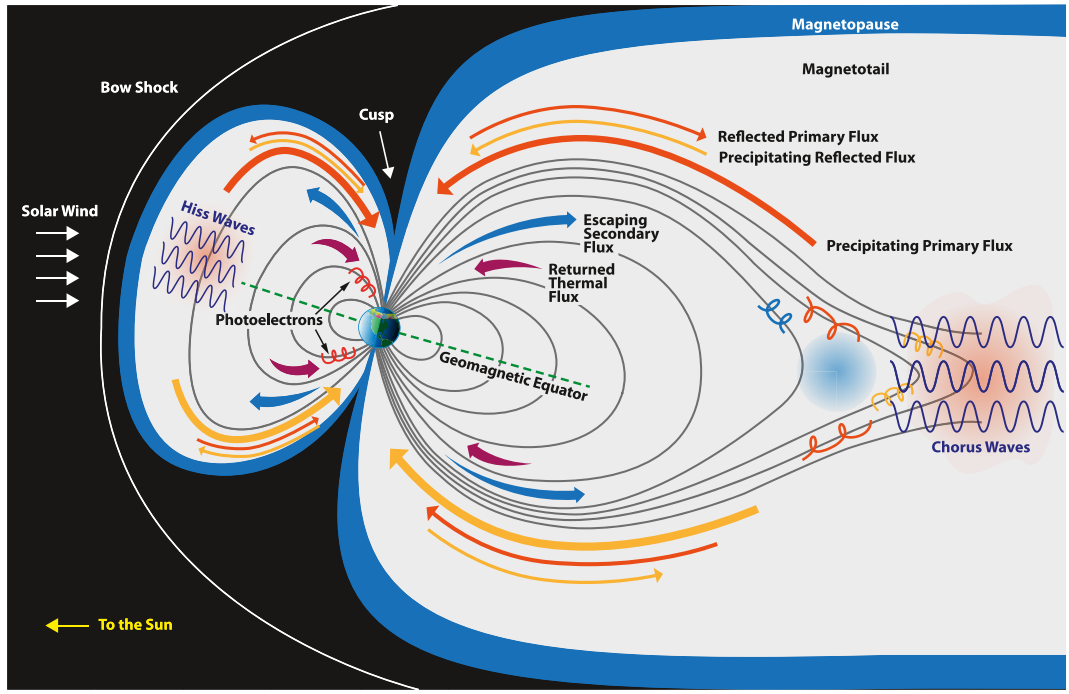

Figure 6. Magnetosphere-ionosphere-atmosphere processes included in tilted magnetic dipole geometry of SuperThermal Electron Transport code.

Essentially, the electron heat flux in the ionosphere is carried by electrons with the energies below 1 eV and this parameter is not measurable explicitly by any existing space plasma techniques: especially in the real event studies that we do in our manuscript. As was noticed by Khazanov at al. (2019), the knowledge of the thermal electron energy flux at the upper ionospheric boundaries is "the Achilles' heel of *all* modern ionospheric models and requires a special consideration." These electron thermal/heat fluxes define the electron temperature profile at the upper ionospheric altitudes and, as a result, the total electron density content that is required for different kinds of space weather applications.

All space plasma events that we discussed in this paper and presented in Section 3 are located on the closed field lines connected with atmospheric magnetic footprints of northern and southern hemispheres. Depending on the season of the year and solar illumination, this creates the different distribution of neutrals and charged populations and has strong influence on MIA energy interplay of SE populations. To account for all these processes, the STET code that we use in our study, is moved to the tilted dipole magnetic field configuration as presented in Figure 6.

4.2. The STET Code: Run Settings

STET code was used in the past in the pure dipole magnetic field configuration to study the interaction of ECH and chorus waves with the Earth's plasma sheet electrons (Khazanov et al., 2015, 2017). It was also used in the similar analysis of the MIA energy interplay driven by time domain structures (TDSs) in the region of the diffuse aurora (Khazanov, Shen, et al., 2021). This SE model has been validated with Fast Auroral SnapshoT (FAST) (Khazanov et al., 2016) and DMSP (Khazanov, Glocer, & Chu, 2021) electron spectra measurements as well as with optical observation by Samara et al. (2017), which ensure its applicability to study the realistic events of the Van Allen Probes observation presented in Section 3.

STET code solves gyro-average kinetic equation for the SE for the energies above 1 eV and its upper energy limit is not restricted because it includes the relativistic effects (Khazanov, 2010). This kinetic equation for the SE that we used in our study can be presented as (Khazanov, Glocer, & Chu, 2021)

$$\frac{1}{v}\frac{\partial \Phi}{\partial t} + \mu\frac{\partial \Phi}{\partial s} - \frac{1-\mu^2}{2}\left(\frac{1}{B}\frac{\partial B}{\partial s} - \frac{F}{E}\right)\frac{\partial \Phi}{\partial \mu} + EF\mu\frac{\partial}{\partial E}\left(\frac{\Phi}{E}\right) = Q + \langle S \rangle \quad (1)$$

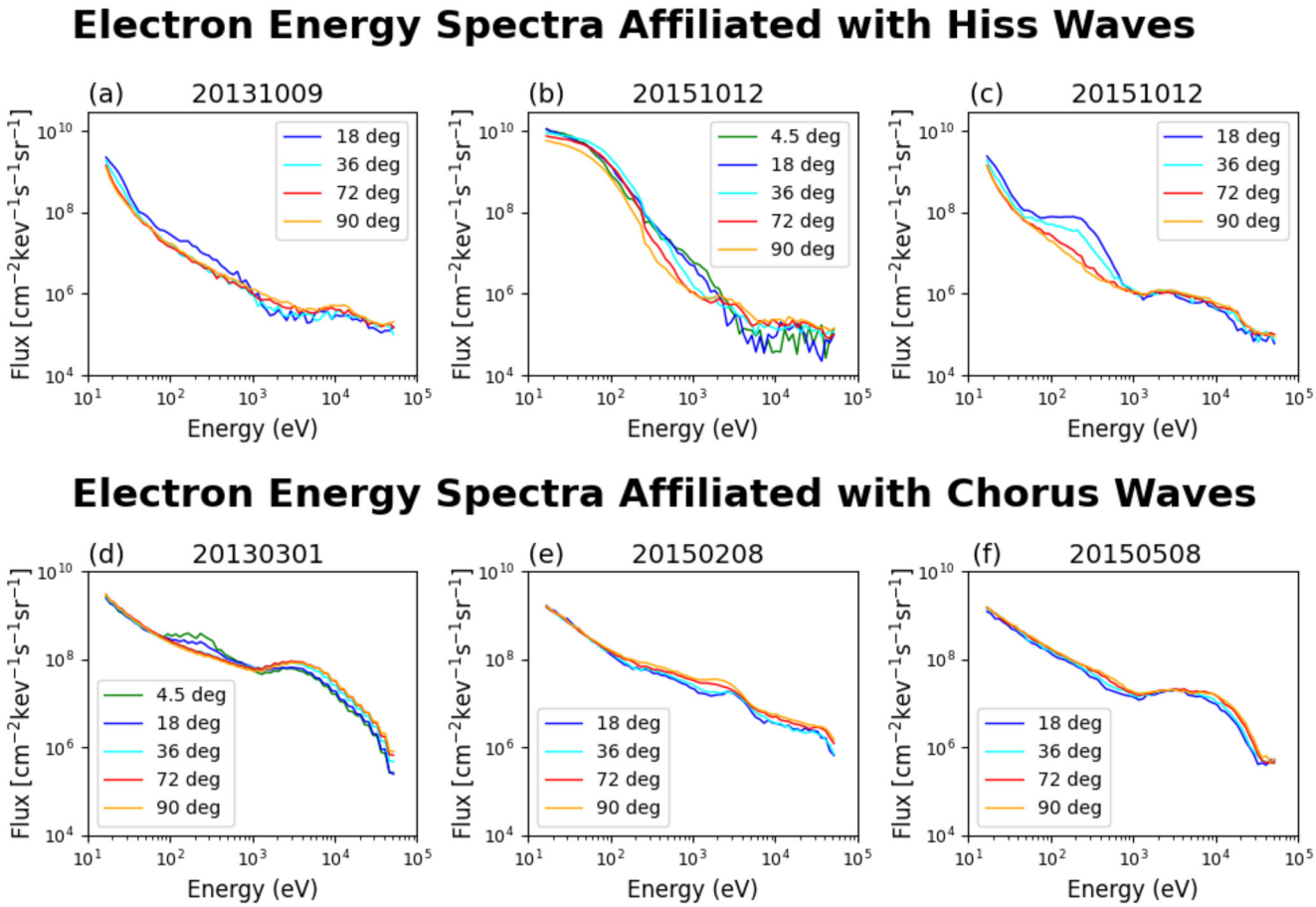

Figure 7. The electron energy spectra of the events measured by Van Allen Probe A, shown for selected pitch-angles for both hiss wave (top) and chorus wave (bottom) events.

where $\Phi = 2Ef/m^2$ is the SE flux, f is the electron distribution of SE and m their mass, B is geomagnetic field, v is SE velocity, t is time, s is the distance along the field line, E is the particle energy, and μ is the cosine of the pitch-angle. F is the electric field force, Q is the SE source term from EUV flux, and $\langle S \rangle$, which includes collision integrals, represents interactions with thermal electrons and ions, scattering with neutral particles, and wave-particle interactions. A detailed derivation of these collisional and wave-particle interaction terms is given in Khazanov (2010) and Khazanov et al. (2015) and all of them are explicitly presented in the recent paper by Khazanov et al. (2020).

As indicated by the title of this manuscript and discussed in the Introduction, the major focus of our study is the estimation of electron thermal heat flux driven by large powerful whistler waves (hiss and chorus) measured by the Van Allen Probes and presented in Section 3. The methodology of STET based heat flux calculation has been discussed in the papers by Khazanov et al. (2019, 2020) and presented in the Appendix A of this paper.

Figure 7 provides the overview of the electron energy spectra during all events presented in Section 3, that were measured by Van Allen Probes and used in our manuscript to assess the value of electron heat fluxes driven by intense whistler waves. We obtained the time averages of electron fluxes at different pitch angles and energies measured by the HOPE instrument during the 5-min intervals in Figures 2 and 4. The 5-min average procedure is consistent with our method to process the wave data and provides smooth electron flux distributions as a function of pitch angle and energy. The observations show little temporal variation of electron flux during the 5-min intervals. Instead of referring to the case study, from now on, we will indicate each case by the date of measurements of these fluxes. Such an approach will visually help the reader identify the selected event in the STET code with driving simulation parameters for the empirical plasma and neutral atmosphere models, as well as solar fluxes and conditions of illumination in the northern and southern hemispheres.

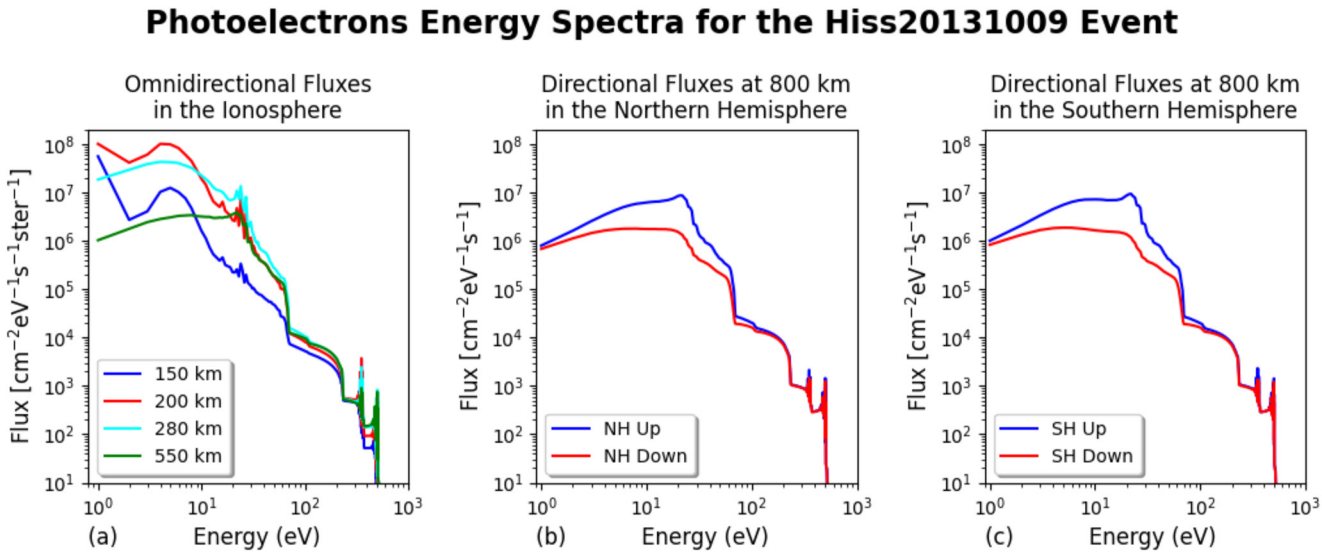

Figure 8. Photoelectron fluxes for the Hiss event of 2013109 when magnetically conjugate ionospheres were illuminated. Panel (a) illustrates the typical altitudinal variation of photoelectron omnidirectional fluxes, and panels (b and c) show directional photoelectron fluxes at 800 km in the Northern and Southern hemispheres, correspondingly.

The top panels of Figure 7 show the electron energy spectra associated with hiss waves and the button ones with chorus waves selected for our heat flux analysis. These energy spectra are shown for the different pitch angles as provided by Van Allen Probes observations. These energy spectra and the associated whistler wave activity are fairly steady up to several tens of minutes, compared to the time (2–3 min) of electron thermal flux formation that we studied in the past (Khazanov et al., 2020) and presented in the Appendix A.

Taking into account these above-mentioned timescale considerations, STET code was set up to run in the steady-state regime. It means that for each case presented in Figure 7, SE magnetospheric trapped population was selected to be as shown in the window that represents selected case study and let WPI processes to move this population into the loss cone, followed up by MIA SE energy interplay and formation of electron thermal heat fluxes. The simulations that are presented below were performed in the tilted dipole magnetic field geometry as it is shown in Figure 6 and used the following inputs to the STET model. The neutral atmospheric model used is the MSIS-90 (Hedin, 1991). The plasma density structure in the ionosphere is based on the IRI-2016 model (Bilitza et al., 2017), and extended into the magnetosphere based on electron density measurements presented in Section 3. Cross sections for elastic collisions, state-specific excitation and ionization were taken from Solomon et al. (1988).

5. SE Energy Spectra and Affiliated Heat Fluxes

In this paper, we analyze the electron precipitation dynamics due to the strong hiss and chorus waves in the presence of ionospheric photoelectrons. Production of ionospheric photoelectrons is the result of the interaction of Solar UV and X-ray radiation with the neutral atmosphere and their energy spectra variation requires independent clarification. As an example, Figure 8 shows photoelectron fluxes for the Hiss event of 20131009 when magnetically conjugate ionospheres were illuminated. The first panel illustrates the typical altitudinal variation of photoelectron omnidirectional fluxes, and two other panels show directional photoelectron fluxes at 800 km in the northern and southern hemispheres, respectively. We use only this event as independent photoelectron simulation to illustrate the features of electron spectra. All other simulations presented below show electron energy spectra that are driven by WPI processes in the presence of photoelectron production if these are available in some of the magnetically conjugate regions.

The altitudinal variations of photoelectron energy spectra have common feature that always will be present in the superthermal electron flux analysis that will be discussed here. Among them are flux enhancement near these energies, 300–500 eV, coming from Auger ionization of neutral particles N_2 and O by solar irradiance between

1.5 and 3 nm, and the drop near 60 eV coming from a sharp drop in solar irradiance below 16 nm (Khazanov et al., 2014). There are also some additional peculiarities of the photoelectron energy spectra; the trough feature at the low altitudes (below 200–250 km) between 2 and 3 eV coming from losses of photoelectrons in the excitation of N_2 vibrational levels. This feature will not appear in the fluxes presented in the follow-up subsections because the focus of our manuscript is different. There are also spikes between 20 and 30 eV coming from photoionization of O and N_2 by the strong 30.4 nm (40.8 eV) irradiance (Khazanov, 2010; Khazanov et al., 2014). These features will be present on some of the plots presented below, depending on the plasma density structure between the two magnetically conjugate regions.

5.1. Hiss Waves Driven SE and Electron Heat Energy Fluxes

The most intense hiss wave activity and SE fluxes are typically present in the plasmaspheric plumes where magnetospheric core plasma densities are locally elevated (Ma et al., 2021). The hiss waves selected in Figure 3 have higher wave amplitudes than the statistical hiss wave amplitude during disturbed conditions of AL* < -500 nT (W. Li et al., 2015). The hiss waves are also modulated by the density structures, showing higher wave power in higher density region possibly due to the wave amplification and focused ray propagation (Chen, Thorne, et al., 2012).

Assuming that the magnetospheric trapped electrons are scattered by hiss waves as presented on the upper panel in Figure 7, STET code was run in the tilted dipole magnetic field configuration as presented in Figure 6. Each hiss wave run case is dated, presented in Figure 9, and shows downward and upward SE fluxes (first and second columns) and their ratios (third column) at the altitude of 800 km in the northern (PN_{up}, PN_{dn}) and southern (PS_{up}, PS_{dn}) hemispheres.

Hiss 20131009 case was already shown in Figure 8 for the demonstration purpose of photoelectron spectra features and is presented by the upper three panels in Figure 9. This figure as well as the other plots presented below, takes into account WPI that drives trapped electron populations (shown in Figure 7) into the loss cones of both magnetically conjugate regions. This, and two other cases, 20151009 and 20151012, have some of the differences and similarities in the electron energy spectra behavior. All hiss wave cases in Figure 9 show a very slight difference between downward and upward fluxes as well as their UP/DN ratios in the northern and southern magnetically conjugate regions. Because of the elevated cold plasma densities between the magnetically conjugate regions, all hiss cases lost spikes between 20 and 30 eV coming from photoionization of O and N_2 by the strong 30.4 nm (40.8 eV) irradiance.

There are also noticeable differences between all hiss-driven SE fluxes in Figure 9. Among them are: (a) Flux intensities and different transitional energies where upward flux dominates over the downward one; (b) Different shapes of UP/DN ratios; (c) Cases 20151009 and 20151012 lost the SE intensity drop near 60 eV and their Auger N_2 and O spikes are diminished compared to the hiss event of 20131009, indicating smaller role of ionospheric photoelectrons in the formation of their SE energy spectra. Event 20131009 compared to two other cases has a relatively large difference in UP/Down ratios that reaches more than a factor of 5 around the energy of 20 eV, which indicates the possibility of plasma instability development that is out of scope of this paper and would require a more focused study of this process.

SE distribution function that is presented and discussed in Figures 8 and 9 is shown at upper ionospheric altitude of 800 km. This altitude seamlessly separates ionosphere and magnetosphere because STET code considers these two areas as one single region that is located between two altitudes of 90 km in the northern and southern hemispheres. The SE fluxes presented in Figures 8 and 9 are the result of magnetosphere-ionosphere-atmosphere energy interplay with participation of the two magnetically conjugate regions as shown in Figure 6. The Coulomb interaction of SE with the thermal electrons at magnetospheric altitudes forms the electron heat fluxes that is the major focus of our studies presented in this paper. It is constructive to show SE fluxes in the magnetosphere and close the loop of heat flux calculation presented in the Appendix A of this paper.

Continuing the discussion of hiss-driven SE cases, Figure 10 shows more global view of SE fluxes as a function of distance along the magnetic field line, and their velocity space characteristics. Figure 10 has a similar organization showing each hiss case by three different rows in the same order as simulations presented in Figure 9. The first column presents SE omnidirectional fluxes along the magnetic field line from 150 km to the magnetic equator. The second column demonstrates pitch-angle/energy configurations at the magnetic equator that correspond

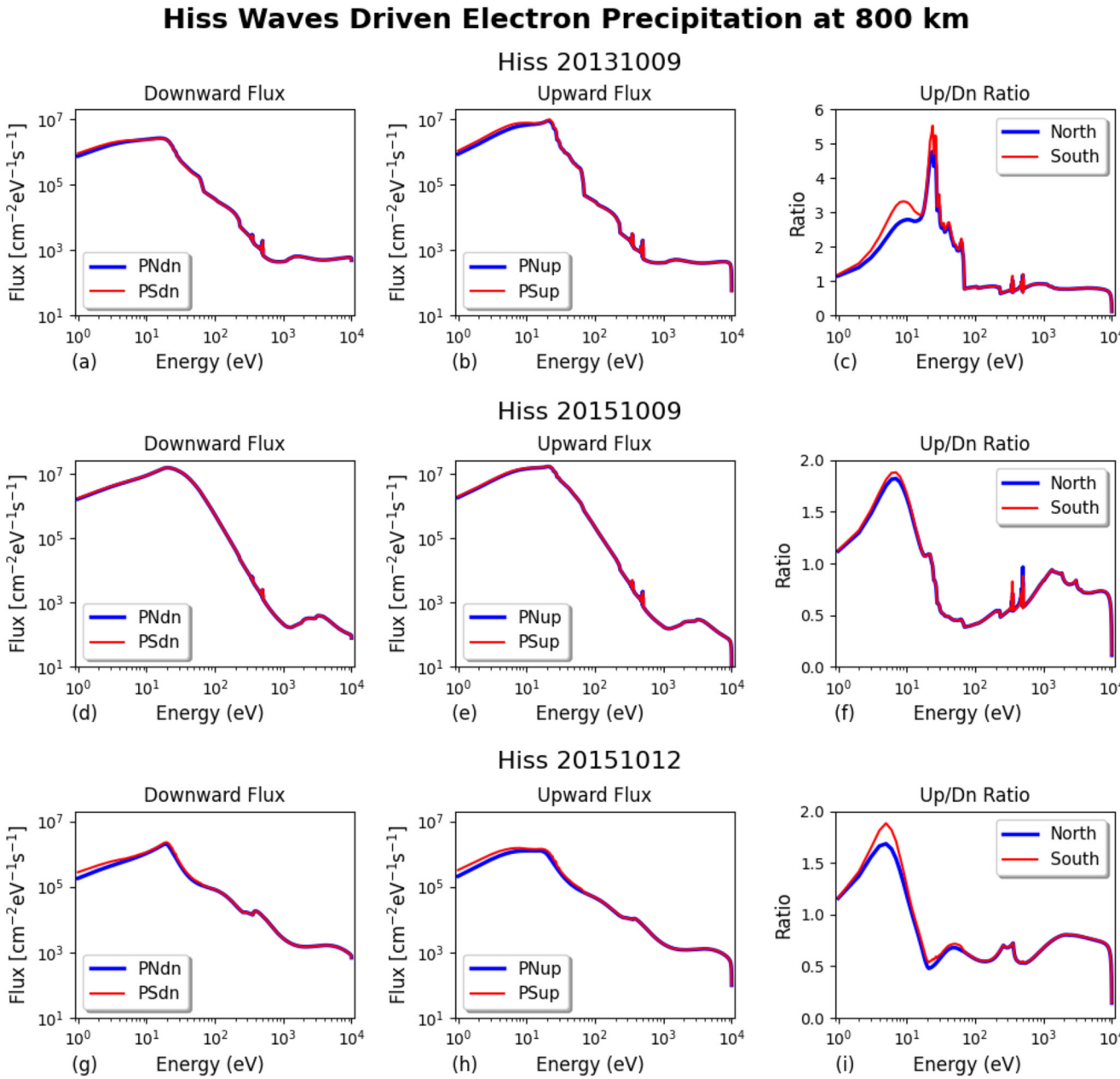

Figure 9. The downward fluxes, the upward fluxes, and their ratios for the three hiss wave cases, (a–c) 20131009, (d–f) 20151009, and (g–i) 20151012.

to the hiss events of 20131009, 20151009, and 20151012. Finally, the third column shows equatorial energy distribution for the pitch angles of 0°–90°.

The simulation output and some plotting scales in Figure 10 are chosen in a way to survey and to show prominent features of electron distribution function. This includes irregular distance grids for the first column (*y*-axis) with finer spacing at lower distances, finer grids at lower energies in the second column (*x*-axis) and irregular pitch-angle intervals in the third column (*x*-axis). This, however, shows pretty accurate representation of the line plots that are shown in Figure 9. For example, comparison of the energy spectra at 800 km altitude using first windows of Figure 9 for the simulation case of 20131009 shows that the highest SE flux is around 10 eV, peaking at above 10^6 cm^{-2} s^{-1} sr^{-1} eV^{-1} (light red color), then steadily drops. Further, toward the higher energies, SE flux stabilizes starting at 1 keV energy, at about 300 cm^{-2} s^{-1} sr^{-1} eV^{-1} (light blue color). At distances beyond 800 km, the omnidirectional fluxes at low energies reach four orders of magnitude weaker but shows similar

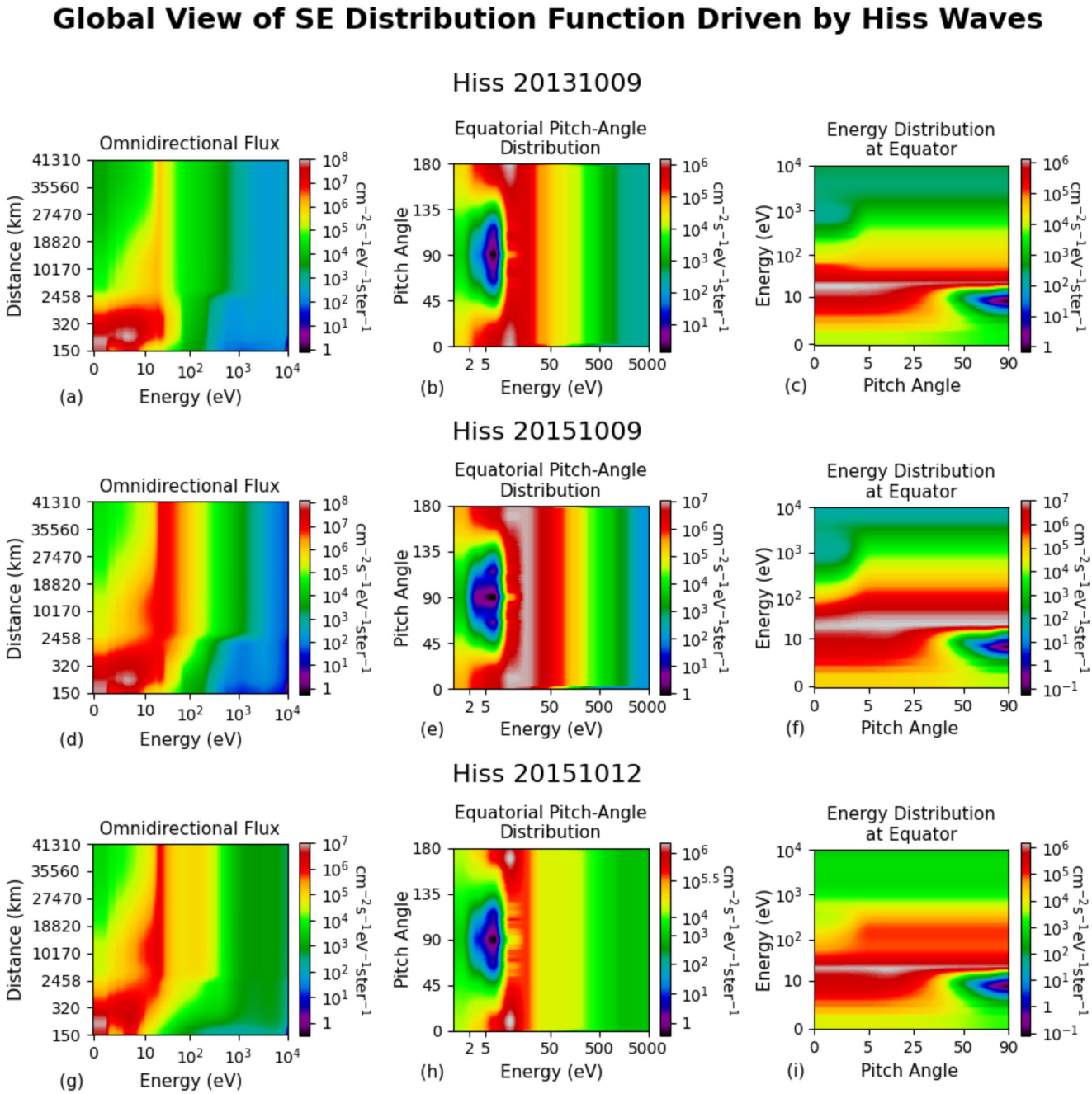

Figure 10. The global view of superthermal electron (SE) fluxes for the three hiss cases as correspondingly shown in Figure 9. The first column (a, d, and g) shows SE omnidirectional fluxes from 150 km to the top of corresponding field lines, the second column (b, e, and h) demonstrates pitch-angle/energy configurations on the top of geomagnetic field lines, and the third column (c, f, and i) shows equatorial energy distribution for the pitch-angles of 0–90°.

drop off behavior for energies above 60 eV indicating photoelectron energy spectra behavior as presented and discussed in Figure 8.

The equatorial pitch-angle distributions show a minimum of flux of 1 cm^{-2} s^{-1} sr^{-1} eV^{-1} and below occurring around 10 eV and 90° pitch-angle, and the fluxes steeply rise to more than 10^6 $cm^{-2}s^{-1}sr^{-1}$ eV^{-1} away from this minimum for different pitch-angles and energies. Such a nonmonotonic behavior of SE flux indicates the possibility of plasma instability that would be addressed in our future studies. For higher energies above 20 eV, the flux drop-off behavior shows no dependence on pitch angles. The energy distribution at equator appears consistent with the equatorial pitch-angle distribution, including a flux minimum of about 1 $cm^{-2}s^{-1}sr^{-1}$ eV^{-1} at 90°

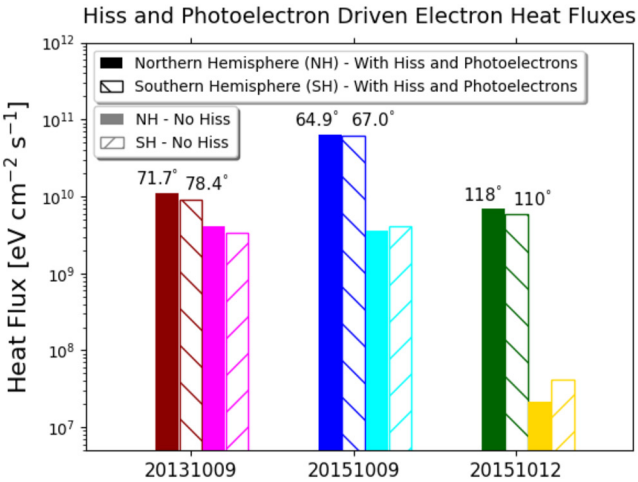

Figure 11. The combined effect of hiss waves and photoelectron driven electron heat fluxes for the three selected hiss cases, for electron heat fluxes coming from the magnetosphere at the upper ionospheric altitude of 800 km. Brown, blue, and green bars correspond to the cases when hiss-driven and photoelectron precipitations are considered. Pink, light blue, and yellow bars are cases when only photoelectrons are considered.

pitch-angle and energy of 10 eV. We return to the discussion of SE fluxes at magnetospheric altitudes in Subsection 5.2 when the chorus driven electron heat fluxes will be considered.

Coming up to the main topic of our manuscript, Figure 11 presents the combined effect of hiss waves and photoelectron driven electron heat fluxes calculated using STET code-based methodology that is outlined in Appendix A. Here we present all three selected cases that were considered above in our analysis of SE fluxes driven by hiss wave activity and show electron heat fluxes coming from the magnetosphere at the upper ionospheric altitude of 800 km. Each simulation scenario is indicated in Figure 11 by the date and color, and different types of the bars correspond to the northern (solid color bars) and southern (striped same-color bars) hemispheres. Brown, blue, and green bars correspond to the cases when all processes of electron heat flux formation are considered: hiss-driven SE magnetospheric precipitation and photoelectrons escaping from ionosphere. Pink, light blue, and yellow bars correspond to the simulation scenarios, without hiss-driven precipitation, when only photoelectrons participate in the core magnetospheric plasma electron heating.

The way how these electron heat fluxes form by ionospheric photoelectrons and hiss-driven electron precipitation is very similar. Escaping from ionosphere to the magnetosphere, photoelectrons move in inhomogeneous Earth's magnetic field in the narrow (1°–2°) loss cone, and experience small Coulomb collisional scattering toward the trapped zone, interacting with the thermal electrons. In the closed magnetospheric magnetic field configuration that is shown in Figure 6, some of these photoelectrons can become trapped and bounce between the reflection points, continuously losing their energy by heating background magnetospheric electrons and form electron conductivity heat flux. The detailed qualitative and quantitative analysis of this trapping process is given in Khazanov (2010).

Another portion of this heat flux is from the hiss wave-driven electron precipitation to the atmosphere that is labeled in Figure 6 as *Precipitated Primary Flux*. Some portion of this flux dissipates in the atmosphere via ionization of the neutral ionospheric particles, and the rest of this precipitation (*Reflected Primary Flux*) returns to the magnetosphere and travels down to the magnetically conjugate region experiencing additional dissipation on the neutral particles, production of the secondary electrons, and neutral atmospheric backscatter. The above outlined SE dynamics happens simultaneously in two magnetically conjugate regions, and they both participate in the formation of *Escaping Secondary Flux* that is shown in Figure 6 (Khazanov, Glocer, & Chu, 2021). The secondary electron flux has the same energy range $E < 500$ eV as escaping photoelectrons, and their energy deposition processes to the thermal electron population, magnetospheric trapping, and formation of the heat flux are identical to the photoelectron source (Khazanov, 2010; Khazanov et al., 2014). *Return Thermal/Heat Flux* that is produced by photoelectrons and hiss-driven electron precipitations is shown in Figure 6 by purple arrows.

Because the SE transport Equation 1 is a linear differential equation (see details in Khazanov, 2010; Khazanov et al., 2014), we were able to separate photoelectrons and WPI-driven precipitated electron contributions to the electron heat flux formation. As shown in Figure 11, the largest effect is the dominated one in all hiss-driven electron precipitation. In the case of 20131009, however, photoelectrons generated heat fluxes which are close to those driven by electron precipitation. All other heat flux cases, 20151009 and 20151012, are visibly driven by hiss generated electron precipitation. The intensities of the electron heat fluxes coming to both magnetically conjugate regions are very close to each other (like downward and upward SE fluxes that are shown in Figure 9) for all simulation scenarios and are the most intense for the case of 20151009. We will provide additional discussions of the heat electron flux intensities in Section 6 and their consequences on electron temperature formation at upper ionospheric altitudes.

5.2. Chorus Waves Driven SE and Electron Heat Energy Fluxes

We selected three chorus wave events with strong intensities as discussed in Section 3. During the case of 20130301 (Figures 5a–5d), the LBC waves at frequencies below $0.5f_{ce}$ cause the electron pitch-angle scattering

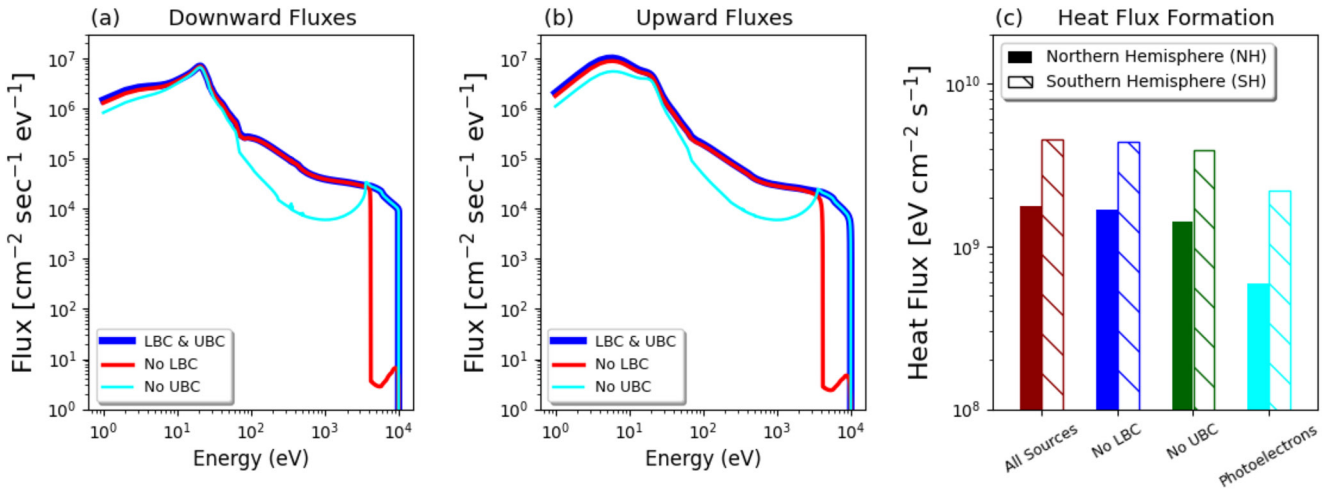

Figure 12. (a) The downward fluxes, (b) the upward fluxes, and (c) the relative contributions of lower-band and upper-band waves in the formation of superthermal electron precipitated and electron thermal heat fluxes at upper ionospheric altitude of 800 km during the chorus case of 20130301.

at energies above ~3 keV. However, as the weaker wave power extends to ~0.7f_{ce}, the UBC waves reduce the minimum resonance of electrons to ~50 eV at the equator although the scattering rates are small. During the case of 20150203 (Figures 5e–5h), the LBC and UBC waves have comparable intensities and cause the electron scattering above 5 keV and at 0.1–5 keV energies respectively. During the case of 20180508 (Figures 5i–5l), the chorus waves are only observed in the lower band, which mainly resonate with electrons at 2–30 keV energies through Landau resonance.

The three cases of magnetospheric electron energy spectra affiliated with intense chorus waves that we use in the settings of STET code are dated and shown on the lower panels in Figure 7. Colored lines in the panels show the electron energy spectra of different pitch angels measured by the Van Allen Probes HOPE instrument. Before discussing each case, in Figure 12 we analyze the relative contributions of LBC and UBC waves in the formation of precipitated SE and electron thermal heat fluxes at upper ionospheric altitude of 800 km during the chorus case of 20130301.

The scenario that is presented in Figure 12 demonstrates the effectiveness of each of the chorus branches in simulated studies presented below. Figure 12a shows downward and Figure 12b shows upward fluxes in the northern hemisphere. In all cases presented here the contribution of photoelectron was considered and the only difference was made by turning on and off LBC and UBC chorus branches. As it is clearly seen from these simulated cases, LBC wave influences energy spectra above 4 keV, and UBC modifies the SE energy range below 4 keV, down to the energies of about 100 eV. These energy ranges of LBC and UBC wave contributions are consistent with the energies of their diffusion coefficients shown in Figures 5a–5d and discussed above. The hot electron fluxes presented in Figure 12c show corresponding variation of these values for northern and southern hemispheres when LBC and UBC waves "work" together or one turned off. As one can see from these results, heat fluxes practically remain the same in both magnetically conjugate regions when one of these chorus branches is absent. This is because the SE fluxes in the energy range below 100 eV is the major contributor to the heat flux formation (shown in first and second panels) and remains to be unchanged when one of the chorus branches was absent. However, for this case study, 20130301, if chorus waves are completely absent and only photoelectrons are considered (light blue photoelectron case in Figure 12), the total hot electron flux will drop by a factor of 2–3 depending on photoelectron production in magnetically conjugate regions.

From the logic of the previous subsection where hiss waves were used to drive the SE precipitation, we consider the magnetospheric trapped electron population presented by the lower panels in Figure 7 and perform STET simulations using the configuration settings as presented in Figure 6. Each chorus wave run case is dated and presented in Figure 13 and shows downward and upward SE fluxes (first and second columns) and their ratios (third column) at the altitudes of 800 km in the northern (PN_{up}, PN_{dn}) and southern (PS_{up}, PS_{dn}) hemispheres.

Compared to the hiss cases presented in Figure 9, chorus-driven SE fluxes for all cases of 20130301, 20150203, and 20180508, have more pronounced hemispheric asymmetry of downward and upward SE fluxes, and their

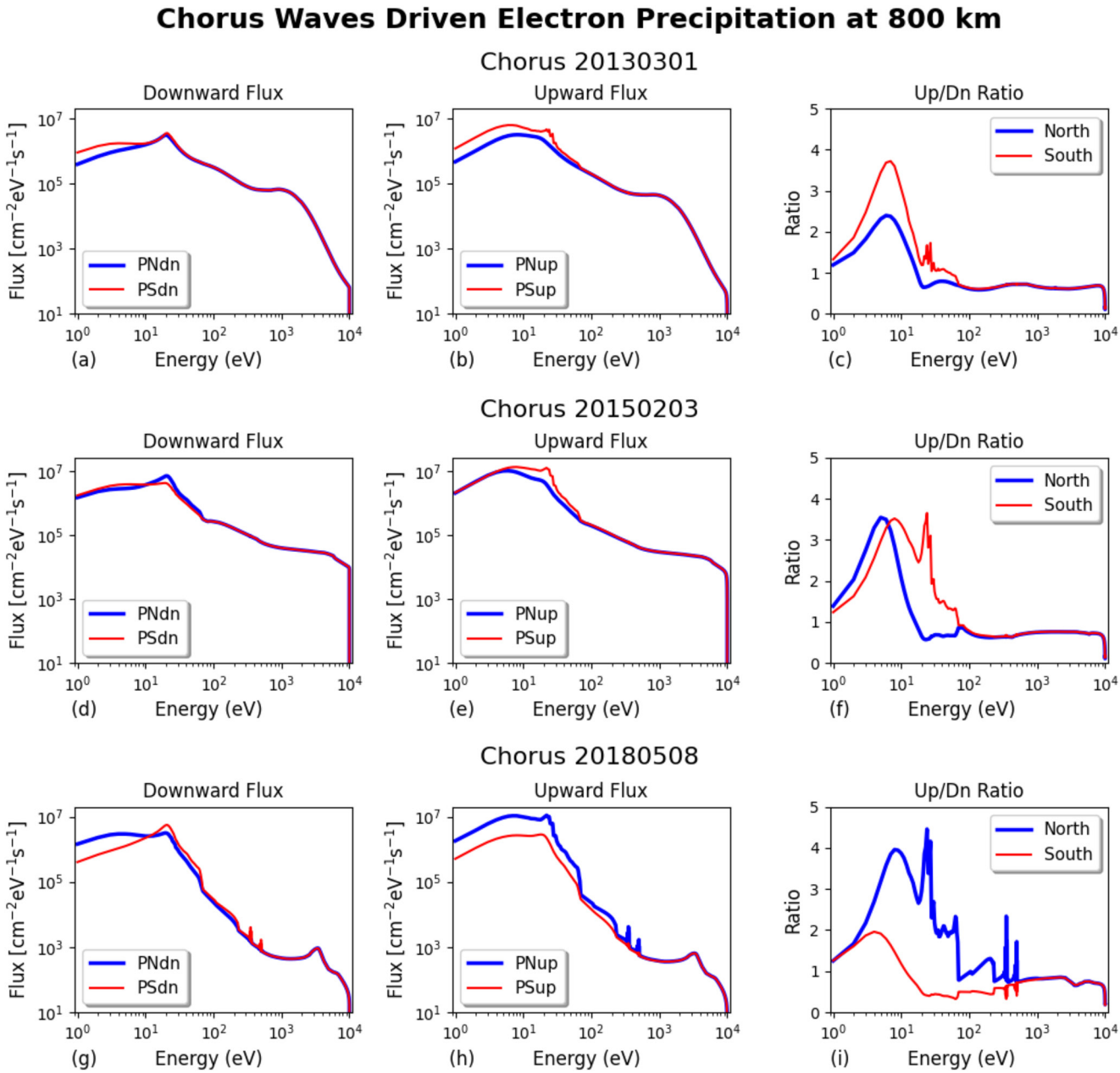

Figure 13. The downward fluxes, the upward fluxes, and their ratios for the three chorus wave cases, (a–c) 20130301, (d–f) 20150203, and (g–i) 20180508.

ratios at the altitude of 800 km. Upward fluxes of all chorus simulations have traces of photoelectron energy spikes between 20 and 30 eV coming from photoionization of O and N_2 by the strong 30.4 nm (40.8 eV) irradiance. The Auger spikes, however, and the drop near 60 eV that comes from a sharp drop in solar irradiance below 16 nm are only present in the simulation scenario of 20180508. All these features also show explicitly pronounced UP/DN flux ratios presented in the third column of each case. As in the hiss wave cases in Figure 9, there are noticeable differences between upward and downward SE fluxes. The energy range of these ratios is much broader compared to the hiss-driven precipitation ones and can cause plasma instabilities.

As it was discussed in the case of the hiss waves presented in Subsection 5.1, and outlined in the Appendix A of this paper, the Coulomb collisional processes between SE and cold electrons at magnetospheric altitudes are the major contributors to the electron heat flux formation. Therefore, it would be legitimate to demonstrate the SE fluxes at magnetospheric altitudes driven by chorus waves.

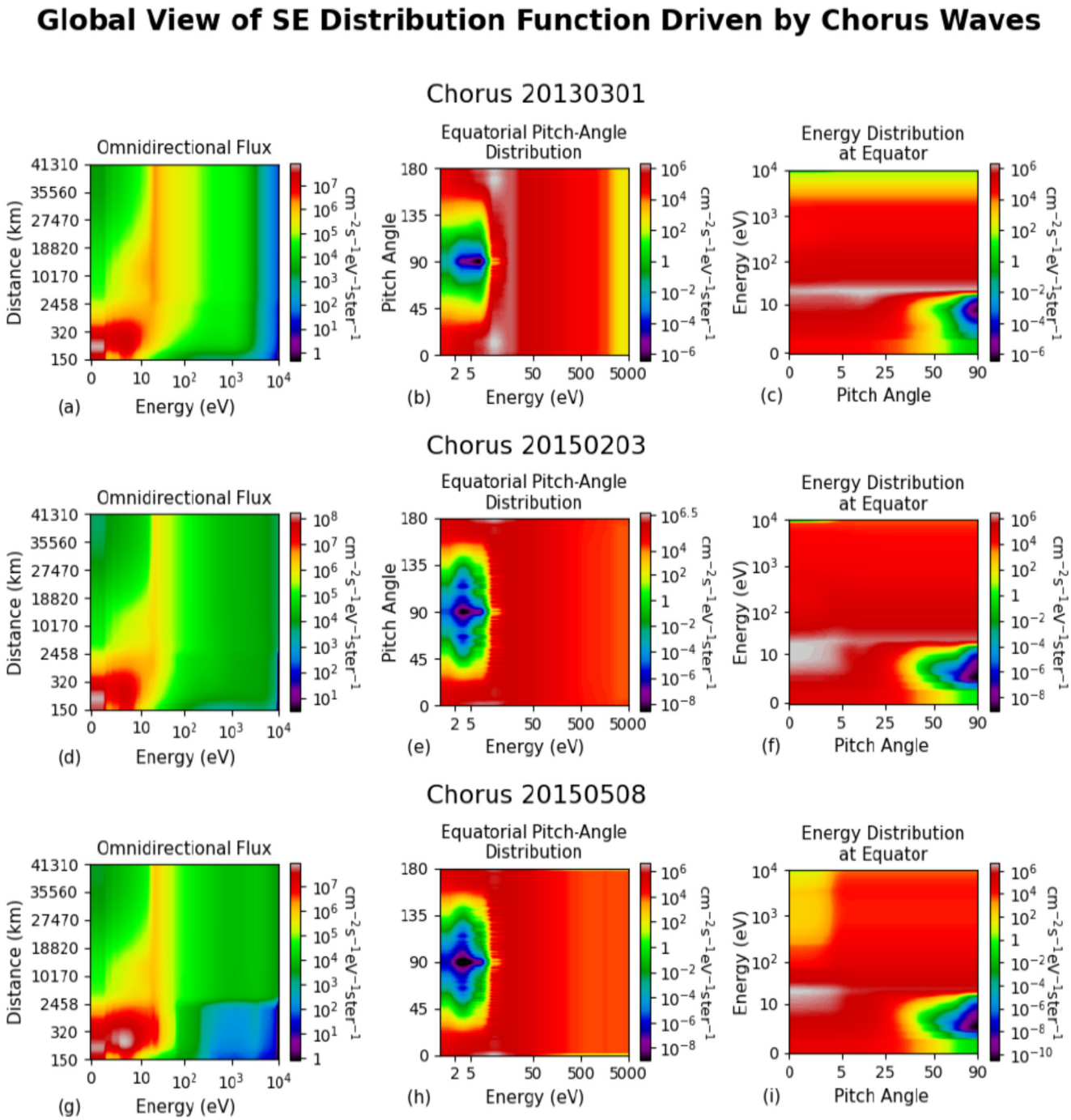

Figure 14. The global view of superthermal electron (SE) fluxes for the three chorus cases as correspondingly shown in Figure 13. The first column (a, d, and g) shows SE omnidirectional fluxes from 150 km to the top of corresponding field lines, the second column (b, e, and f) demonstrates pitch-angle/energy configurations on the top of geomagnetic field lines, and the third column (c, f, and i) shows equatorial energy distribution for the pitch-angles of 0–90°.

Distribution slices for the chorus result is presented with the same organization as that of the hiss result. Figure 14 shows a more global view of SE fluxes as a function of distance along the magnetic field line, and their velocity space. The first column presents SE omnidirectional fluxes from 150 km to the top of corresponding field lines. The second column demonstrates pitch-angle/energy configurations on the top of geomagnetic field lines that correspond to the chorus events of 20130301, 20150203, and 20180508. Finally, the third column shows equatorial energy distribution for the pitch-angles of 0–90°.

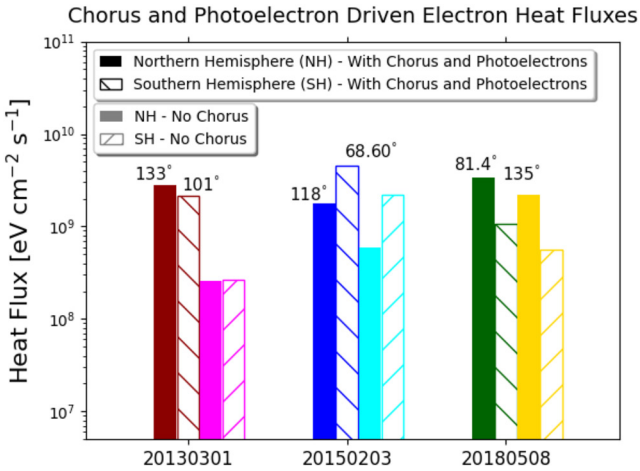

Figure 15. The combined effect of chorus waves and photoelectron driven electron heat fluxes for the three selected chorus cases, for electron heat fluxes coming from the magnetosphere at the upper ionospheric altitude of 800 km. Brown, blue, and green bars correspond to the cases when chorus-driven and photoelectron precipitations are considered. Pink, light blue, and yellow bars are cases when only photoelectrons are considered.

The simulation output and some plotting scales in Figure 14 are chosen in a way to survey and to show prominent features of electron distribution function. It is done in the same format as for the cases with hiss wave activity presented in Figure 10. This includes irregular distance grids for the first column (y-axis) with finer concentration at lower distances, finer grids at lower energies in the second column (x-axis), irregular pitch-angle intervals in the third column (x-axis), and lastly the color scale of the equatorial pitch-angle distribution for the 20150203 event is also adjusted to better display the change in high fluxes. This, however, accurately represents the line plots that are shown in Figure 13. For example, comparison of the energy spectra at 800 km altitude using first windows in Figures 13 and 14 for the simulation case of 20130301 shows that the highest SE flux is around 10 eV, peaking at above 10^7 cm^{-2} s^{-1} sr^{-1} eV^{-1} (light red color), then steadily drops. Furthermore, toward the higher energies, SE flux shows a steeper decline starting at 1 keV and dropping below 500 cm^{-2} s^{-1} sr^{-1} eV^{-1} for energies above 5 keV (light blue color). For distances beyond 800 km, the omnidirectional fluxes show similar drop-off behavior for energies above 60 eV that represents the behavior of photoelectron energy spectra as in Figure 8.

The equatorial pitch-angle distributions show a flux minimum of 10^{-6}–10^{-8} cm^{-2} s^{-1} sr^{-1} eV^{-1} occurring around 10 eV and 90° pitch-angle, and the fluxes steeply rise over 12 orders of magnitude to around 10^6 away from this minimum for different pitch-angles and energies. For higher energies above 20 eV, the flux drop-off behavior shows no dependence on pitch angles. The energy distribution at equator appears consistent with the equatorial pitch-angle distribution, including a flux minimum as low as 10^{-6} cm^{-2} s^{-1} sr^{-1} eV^{-1} or lower at 90° pitch-angle and energy of 10 eV. Although showing similar trends as in hiss, chorus events have the salient features of low-flux magnitude, that is as low as 10^{-8} cm^{-2} s^{-1} sr^{-1} eV^{-1}, for the equatorial result compared to that of hiss events.

Magnetospheric SE fluxes presented in Figure 10 driven by hiss waves and in Figure 14 as a result of the chorus wave activities, have many different peculiarities in the configuration and velocity spaces. They both, however, are well-connected with their ionospheric counterparts and accurately represent fluxes at the altitude of 800 km. Nevertheless, some of the features of SE fluxes presented in the pitch-angle energy space, for example, in the vicinity of the energies below 30–40 eV, would require additional plasma stability analysis that is out of the scope of our manuscript.

In the previous subsection we provided the detailed description of the electron heat formation due to SE precipitation driven by hiss waves in the presence of ionospheric electrons. These heat fluxes form in the same way when the chorus waves drive the WPI. Figure 15 presents the combined effect of chorus waves and photoelectron driven electron heat fluxes, calculated using STET code-based methodology that is outlined in Appendix A. Here we present all three selected chorus events, 20130301, 20150203, and 20180508 that were considered above in our analysis of SE fluxes driven by chorus wave activity and show electron heat fluxes coming from the magnetosphere at the upper ionospheric altitude of 800 km. Each simulation scenario is indicated in Figure 15 by the date and color, and different types of the bars correspond to the northern (solid color bars) and southern (striped same color bars) hemispheres. Brown, blue and green bars correspond to the cases when all processes of electron heat flux formation are considered: chorus-driven SE magnetospheric precipitation and photoelectrons escaping from ionosphere. Pink, light blue and yellow bars correspond to the simulation scenarios when only photoelectrons participate in the core magnetospheric plasma electron heating. We used here the same notation as for the case of the hiss events (Figure 11), but for different dates and wave modes.

As in the case of the hiss waves presented in Subsection 5.1, we separated the contribution of photoelectrons and WPI-driven precipitated electrons to the electron heat flux formation. As shown in Figure 15, the later effect is not always the dominating one in the chorus-driven electron precipitation and depends on the illumination conditions in the northern and southern hemispheres. As shown in the chorus simulation scenarios 20150203 and 20180508, for example, there are noticeable differences between incoming electron heat fluxes in magnetically conjugate regions. In the case of the hiss waves, however, these fluxes were almost identical for the northern and southern hemispheres, like in the chorus case of 20130301.

In Section 6, we continue qualitative and quantitative analysis of electron heat flux formation presented in this section and discuss their consequences for the electron temperature formation and MIA energy interchange in space plasma.

6. Discussion

As we emphasized in the previous sections, the major focus of our study is electron heat fluxes generated by intense whistler waves at the upper ionospheric altitudes in the presence of ionospheric photoelectrons. The knowledge of the thermal electron energy flux at the upper ionospheric boundaries is the *Achilles' heel* of all ionospheric models that were pointed out in many papers (Bekerat et al., 2007; Glocer et al., 2012; Richmond et al., 1992; Ridley et al., 2006; Schunk et al., 1986).

The electron heat flux in the ionosphere is carried by electrons with the energies below 1 eV and this parameter is not explicitly measurable by any existing space plasma techniques. The best one can do is to use an implicit calculation of electron heat fluxes using experimental electron temperature profile and the well-known expression for the electron heat flux presented by Banks (1966). Such an approach has been used in the paper by Fallen and Watkins (2013) where they presented long time range electron thermal flux estimation from Poker Flat Incoherent Scatter Radar measurements of electron density and temperature.

As we demonstrated in Section 2, magnetospheric whistler waves, chorus and hiss, can't provide the resonant heating of the core electron plasma population. These both whistler branches, however, can *implicitly* participate in the heating processes of the core plasma thermal electron population by triggering the broad energy range of the electron precipitation from the magnetosphere and follow-up atmospheric ionization processes, production of superthermal electrons, their magnetosphere-ionosphere-atmosphere energy interplay with participation of both magnetically conjugate hemispheres, and their Coulomb interaction with background magnetospheric thermal electrons. Using strong hiss and chorus waves measured by Van Allen Probes presented and discussed in Section 3 and STET simulations presented in Sections 4 and 5, we evaluated the formation of electron heat fluxes at the upper ionospheric altitudes.

In all simulations presented above, STET code was run in the shifted magnetic field dipole geometry as shown in Figure 6. This allows the simulations to catch all peculiarities in the solar illumination conditions in magnetically conjugate regions and corresponding asymmetries of plasma and atmospheric composition. Ionospheric photoelectrons that are produced in magnetically conjugate regions as the result of the interaction of Solar UV and X-ray radiation with the neutral atmosphere, are sensitive to these asymmetries, especially to the conditions of illuminations in northern and southern hemispheres. Their role, however, is very different in the formation of SE and heat electron energy fluxes and depends on the intensity of magnetospheric WPI driver—hiss or chorus waves that are considered in our manuscript.

In the hiss-driven electron precipitation, we presented in Subsection 5.1 WPI processes always dominate in the production of electron heat fluxes; however, the traces of the photoelectrons are always present in SE fluxes. For example, for SE fluxes shown in Figure 9, Hiss 20131009 (with zenith angles in the north of 71.7° and in the south of 78.4°) and Hiss 20151009 (with corresponding angles of 64.9° and 67.0°) cases explicitly show some of the photoelectron features that are presented and discussed in Figure 8. In both cases, photoelectron production was taken place on the illuminated magnetically conjugate points. In the Hiss 20151012 case, however, the northern and southern hemispheres were in the darkness, with zenith angle on the north of 118° and the south of 110°, respectively. Because of this, photoelectron features of the energy spectra of SE practically are diminished. As a consequence, the contribution of photoelectrons to the heat electron thermal flux formation is negligible (Figure 11). Here and below, we show zenith angle values on the top of the color bars that represent the total heat flux calculation with participation of the whistler waves and ionospheric photoelectrons.

The total heat fluxes presented in Figure 11, when both hiss waves and photoelectrons are present, are relatively high, and for the cases of 20131009 and 20151012 are close to 10^{10} eV·cm^{-2}·s^{-1}. Such magnitudes of the electron heat fluxes can elevate the upper ionospheric electron temperature up to 5000 K. The strongest electron heat flux was calculated for the case of Hiss 20151009 where the heat electron flux almost reaches the value of 10^{11} eV·cm^{-2}·s^{-1} with expecting electron temperature of 10000 K. Here and below, in estimation of electron temperature values in connection with heat fluxes, we use the corresponding analysis presented in the Chapter 6 of the book by Khazanov (2010).

In the cases of the chorus-driven SE precipitation, 20130301, 20150203, and 20180508 presented in Figure 13, the hemispheric asymmetry is more pronounced, and one can see the contribution of photoelectrons to the SE spectra in all these simulation scenarios. The total heat fluxes for all these cases are clearly hemisphere dependent (Figure 15), compared to the corresponding hiss-driven values that are shown in Figure 11. The thermal fluxes of cases 20130301, 20150203, and 20180508 vary as 2×10^9 and 5×10^9 eV cm^{-2}·s^{-1}. Such flux variations at the upper ionospheric altitudes can lead to corresponding Te variations of 3000–4000 K.

The STET code that we used in our studies provide seamless solution of SE fluxes between the two magnetically conjugate regions with lower boundaries at 100 km. It also considers the MIA energy interplay and the communication between the loss cone and the trapped zone, allowing precipitated electrons and photoelectrons to travel multiple times between the northern and southern region, until they completely lose their energy in the magnetosphere and form the electron heat flux that is conducted down to the upper ionospheric altitudes. As we demonstrated in the Appendix A, it takes only about 2–3 min to form this heat flux and reach the steady state solutions, compared to the longer timescale (up to tens of mins) of the electron energy spectra and whistler wave activity that remain almost the same as discussed in Sections 3 and 4. Such a timescale allows drastically simplified heat flux calculations and the usage of steady-state solution of kinetic Equation 1 in the estimation of their values.

The SE distribution function driven by hiss and chorus waves in the presence of photoelectrons presented in Figures 10 and 14 have different and very noticeable peculiarities in the configuration and velocity spaces. Such electron distribution features potentially could lead to the plasma instabilities analysis, like those considered by Mishin (2019) and Mishin and Streltsov (2021) and is out to the scope of this manuscript.

7. Summary

Magnetospheric whistler waves, chorus and hiss, can't provide the resonant heating of the core electron plasma population. However, as we demonstrated in this paper these waves can *implicitly* participate in the heating processes of the core plasma thermal electron population by triggering the broad energy range of electron precipitation from the magnetosphere and follow up atmospheric ionization processes, production of SE population, and their magnetosphere-ionosphere-atmosphere (MIA) energy interplay with participation of both magnetically conjugate hemispheres. This idea of *implicit heating* was proposed by Khazanov et al. (2017, 2020) who used relatively small intensity of chorus and ECH waves with magnitudes of 10 pT and 1 mV/m, respectively. This analysis was performed without any specific affiliated spacecraft data, and with simplified assumptions of Gaussian function to represent wave energy distribution with frequency for both considered waves.

In this manuscript we continued to develop this idea of *implicit heating* thermal electron population by magnetospheric whistlers, using strong hiss and chorus waves measured by Van Allen Probes in the presence of the ionospheric electrons and affiliated realistic wave energy spectra affiliated with these observations. As demonstrated in our resonance energy analysis and shown in the event-specific diffusion coefficient calculations, the energy of electron precipitation significantly depends on the frequency of chorus and hiss waves, in addition to the measured ratio between plasma frequency and electron gyrofrequency (f_{pe}/f_{ce}). The electrons at lower energies are scattered into the loss cone when the wave frequency f/f_{ce} is higher or f_{pe}/f_{ce} is higher. Since the electron flux decreases with increasing energy, the waves with higher frequencies or under a high-density background can cause higher number flux of precipitating electrons, although the average energy of precipitation is lower.

As is found in the analysis presented in Section 5, hiss and chorus waves that initiate the precipitation of magnetospheric electrons with energies below 30 keV and follow-up production of the secondary electrons play an important role in the energy balance of ionosphere-magnetosphere system. As discussed in Figures 11 and 15, the electron heat fluxes that are driven by strong hiss and chorus wave activities always dominate over the corresponding fluxes that are produced by photoelectrons and are the systematic regular source of electron heat flux production on the day side (Khazanov, 2010). In the considered strong hiss event of 215109, for example, the wave-driven heat flux is one order of magnitude larger, compared to the corresponding production by photoelectrons, and reaches the dramatic value around 10^{11} eV cm^{-2}·s^{-1}. Therefore, the newly suggested mechanism plays a very an important role in the energy balance of ionosphere-magnetosphere system and must be considered in the ionospheric space weather simulations.

The electron thermal heat flux is not explicitly measurable by space plasma techniques, but this parameter defines the electron temperature profile at the upper ionospheric altitudes and even near the maximum electron density

of the F2 region (Fallen & Watkins, 2013), and, as a result, the total electron density content that is required for different kinds of space weather applications.

It was indicated in the past by Schunk et al. (1986) and remained unchanged till these days, that "for realistic values of the magnetospheric heat flux, the maximum electron temperature ranges from 5000 to 10000 K at 800 km." However, the sources of these "realistic" magnetospheric fluxes were not completely identified and still are the subject of debate in the modern ionospheric studies (Khazanov et al., 2020, and references therein). As we mentioned in the discussion section, the range of Te variations that our *new approach* gives result of 5000 to 10000 K is consistent with the requirements that come from the ionospheric observations of electron temperature and simulations presented by Schunk et al. (1986).

Appendix A

A1. Electron Heat Flux Calculation

Electron heat flux entering upper ionospheric altitude was calculated using STET based methodology presented by Khazanov et al. (2019, 2020) by integrating the electron-electron and electron-ion collisional term entering SE kinetic Equation 1 over the velocity space:

$$\langle S_{ee}\rangle + \langle S_{ei}\rangle = An_e\left\{\frac{\partial}{\partial E}\left(\frac{\Phi}{E}\right) + \frac{1}{2E^2}\frac{\partial}{\partial \mu}\left[\left(1-\mu^2\right)\frac{\partial \Phi}{\partial \mu}\right]\right\} \tag{A1}$$

where $A = 2\pi e^4 \ln\Lambda$, $\ln\Lambda$ is the Coulomb logarithm, $n_e(s)$ is thermal plasma density, $\Phi = \Phi(s, E, \mu)$ is SE flux. Such an integration of Equation A1 over the energy and pitch-angle variables leads to the expression of SE energy deposition to the thermal electron per unit volume per second as

$$Q_e(s) = 4\pi A n_e(s)\left[\Phi_0\left(E_{\min}\right) - \Phi_0\left(E_{\max}\right) + \int_{E_{\min}}^{E_{\max}} \frac{\Phi_0(E)}{E} dE\right] \tag{A2}$$

Here Φ_0 is SE omnidirectional flux, and $E_{\min}$ and $E_{\max}$ are taken as 1 eV and 10 keV, correspondingly.

The result of integrating Equation A2 along the field line from the geomagnetic equator, s_{eq}, to the upper ionospheric boundary, s_i, represents the incoming electron heat flux entering upper ionospheric altitude

$$q(s_i) = \int_{s_{eq}}^{s_i} Q_e(s)\frac{B_i}{B(s)} ds \tag{A3}$$

presented and discussed in Sections 4–6 of this manuscript. It should be noted that magnetospheric part of the SE distribution function presented in Figures 10 and 14 is the major contributor to electron heat fluxes.

It should be noted that electron thermal flux calculation presented in this Appendix A (Khazanov et al., 2019, 2020), offers a rigorous and systematic theoretical framework to calculate this value and does not depend on any assumption regarding the form of the core electron distribution function.

A2. Heat Flux Temporal Dynamics

Figure A1 demonstrates the temporal dynamics of electron heat flux calculation for different precipitated electron distribution functions and escaping to the magnetosphere photoelectrons. According to McIntosh and Anderson (2014), the most observed electron distribution functions in aurora are:

$$\Phi(E) = AE\exp\left(-\frac{E}{E_0}\right) \tag{A4}$$

$$\Phi(E) = AE\left(1 + \frac{E}{\kappa E_0}\right)^{-\kappa-1} \tag{A5}$$

$$\Phi(E) = A\exp\left(-\frac{(E-E_0)^2}{2\sigma^2}\right) \tag{A6}$$

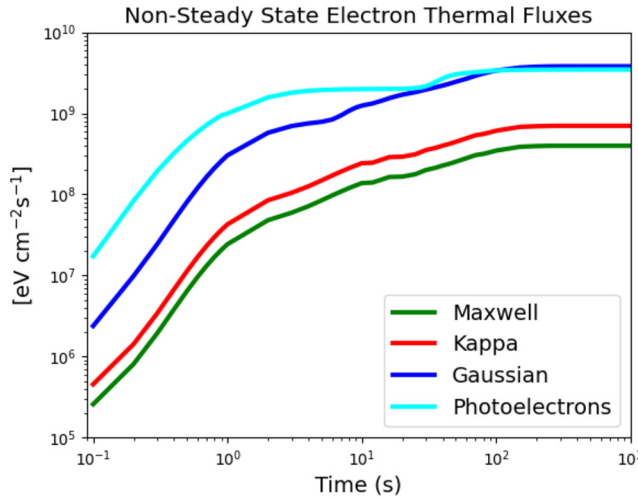

Figure A1. The temporal dynamics of electron heat flux calculation for three different precipitated electron distribution functions and photoelectrons escaping to the magnetosphere.

which are Maxwellian (Equation A4), Kappa (Equation A5), and Gaussian (Equation A6) distribution functions, respectively. $\Phi(E)$, E_0, A, and σ are differential number flux, auroral characteristic energy, normalization constant, and $\sigma = 0.1E_0$ (Banks et al., 1974), respectively.

In Figure A1 the Gaussian distribution function was selected with characteristic energy of 1 keV, the Kappa distribution function with $\kappa = 3.5$ and $E_0 = 2$ keV, and Maxwellian distribution with $E_0 = 3$ keV. The only common feature in all these functions was the selection of the normalization constants A to provide for all cases *identical* energy fluxes, 1 erg $\cdot$ cm^{-2} $\cdot$ s^{-1}. Analyzing Figure A1 one can see almost identical timescale ($\sim$100 s) in the development of electron heat fluxes when they transition to the steady state conditions. The initial stage of the heat flux development by photoelectrons presented here slightly deviate from the timescales that form precipitated electron fluxes Equations A4–A6, but they reach the steady state level at almost the same time.

The discussion above ensures the applicability of steady state version of STET code in the analysis of electron heat flux formation driven by intense whistler waves.

Data Availability Statement

The authors acknowledge the Van Allen probes data from the EMFISIS instrument obtained from http://emfisis.physics.uiowa.edu/Flight/, data from the ECT instrument suite obtained from https://rbsp-ect.newmexicoconsortium.org/data_pub/, and geomagnetic activity data from http://wdc.kugi.kyoto-u.ac.jp/kp/index.html. The data used in this study are available at the data repository https://doi.org/10.6084/m9.figshare.16822213.

Acknowledgments
G. V. K. was supported by NASA HTMS program under award of 80NSSC20K1276, the MARBLE Project, funded by the NASA Living with a Star (LWS) Strategic Capabilities program, LWS Program under the awards 80NSSC19K0080 and 80NSSC20K1817, and NASA award 80NSSC21K1552. Q. M. would like to acknowledge the NASA grants 80NSSC20K0196, 80NSSC19K0844, 80NSSC20K0698, and 80NSSC19K0845, and the NSF grant AGS-2021749.

References

Agapitov, O., Artemyev, A., Krasnoselskikh, V., Khotyaintsev, Y. V., Mourenas, D., Breuillard, H., et al. (2013). Statistics of whistler-mode waves in the outer radiation belt: Cluster STAFF-SA measurements. *Journal of Geophysical Research: Space Physics*, *118*(6), 3407–3420. https://doi.org/10.1002/jgra.50312

Baker, D. N., Jaynes, A. N., Hoxie, V. C., Thorne, R. M., Foster, J. C., Li, X., et al. (2014). An impenetrable barrier to ultrarelativistic electrons in the Van Allen radiation belts. *Nature*, *515*(7528), 531–534. https://doi.org/10.1038/nature13956

Banks, P. (1966). Charged particle temperatures and electron thermal conductivity in the upper atmosphere. *Annales Geophysicae*, *22*, 557–587.

Banks, P. M., Chappell, C. R., & Nagy, A. F. (1974). A new model for the interaction of auroral electrons with the atmosphere: Spectral degradation, backscatter, optical emission, and ionization. *Journal of Geophysical Research*, *79*, 1459–1470. https://doi.org/10.1029/JA079i010p01459

Bekerat, H. A., Schunk, R. W., & Scherliess, L. (2007). Estimation of the highlatitude topside electron heat flux using DMSP plasma density measurements. *Journal of Atmospheric and Solar-Terrestrial Physics*, *69*(9), 1029–1048. https://doi.org/10.1016/j.jastp.2007.03.015

Bilitza, D., Altadill, D., Truhlik, V., Shubin, V., Galkin, I., Reinisch, B., & Huang, X. (2017). International reference ionosphere 2016: From ionospheric climate to real-time weather predictions. *Space Weather*, *15*(2), 418–429. https://doi.org/10.1002/2016SW001593

Bortnik, J., Chen, L., Li, W., Thorne, R. M., Meredith, N. P., & Horne, R. B. (2011). Modeling the wave power distribution and characteristics of plasmaspheric hiss. *Journal of Geophysical Research*, *116*(A12), A12209. https://doi.org/10.1029/2011JA016862

Bortnik, J., Inan, U. S., & Bell, T. F. (2003). Frequency-time spectra of magnetospherically reflecting whistlers in the plasmasphere. *Journal of Geophysical Research*, *108*(A1), 1030. https://doi.org/10.1029/2002JA009387

Bortnik, J., Li, W., Thorne, R. M., Angelopoulos, V., Cully, C., Bonnell, J., et al. (2009). An observation linking the origin of plasmaspheric hiss to discrete chorus emissions. *Science*, *324*(5928), 775–778. https://doi.org/10.1126/science.1171273

Bortnik, J., Thorne, R. M., & Meredith, N. P. (2008). The unexpected origin of plasmaspheric hiss from discrete chorus emissions. *Nature*, *452*(7183), 62–66. https://doi.org/10.1038/nature06741

Chen, L., Bortnik, J., Li, W., Thorne, R. M., & Horne, R. B. (2012). Modeling the properties of plasmaspheric hiss: 1. Dependence on chorus wave emission. *Journal of Geophysical Research*, *117*(A5), A05201. https://doi.org/10.1029/2011JA017201

Chen, L., Li, W., Bortnik, J., & Thorne, R. M. (2012). Amplification of whistler-mode hiss inside the plasmasphere. *Geophysical Research Letters*, *39*(8), L08111. https://doi.org/10.1029/2012GL051488

Chen, L., Thorne, R. M., Bortnik, J., Li, W., Horne, R. B., Reeves, G. D., et al. (2014). Generation of unusually low frequency plasmaspheric hiss. *Geophysical Research Letters*, *41*(16), 5702–5709. https://doi.org/10.1002/2014GL060628

Chen, L., Thorne, R. M., Li, W., Bortnik, J., Turner, D., & Angelopoulos, V. (2012). Modulation of plasmaspheric hiss intensity by thermal plasma density structure. *Geophysical Research Letters*, *39*(14), L14103. https://doi.org/10.1029/2012GL052308

Cole, K. D. (1965). Stable auroral red arcs, sinks for energy of D_{st} main phase. *Journal of Geophysical Research*, *70*(7), 1689–1706. https://doi.org/10.1029/JZ070i007p01689

Cornwall, J. M., Coroniti, F. V., & Thorne, R. M. (1971). Unified theory of SAR arc formation at the plasmapause. *Journal of Geophysical Research*, *76*(19), 4428–4445. https://doi.org/10.1029/JA076i019p04428

Fallen, C. T., & Watkins, B. J. (2013). Diurnal and seasonal variation of electron heat flux measured with the Poker Flat Incoherent-Scatter Radar. *Journal of Geophysical Research: Space Physics*, *118*(8), 5327–5332. https://doi.org/10.1002/jgra.50485

Fu, X., Cowee, M. M., Friedel, R. H., Funsten, H. O., Gary, S. P., Hospodarsky, G. B., et al. (2014). Whistler anisotropy instabilities as the source of banded chorus: Van Allen Probes observations and particle-in-cell simulations. *Journal of Geophysical Research: Space Physics*, *119*(10), 8288–8298. https://doi.org/10.1002/2014JA020364

Funsten, H. O., Skoug, R. M., Guthrie, A. A., MacDonald, E. A., Baldonado, J. R., Harper, R. W., et al. (2013). Helium, Oxygen, Proton, and Electron (HOPE) mass spectrometer for the radiation belt storm probes mission. *Space Science Reviews*, *179*(1–4), 423–484. 1–62. https://doi.org/10.1007/s11214-013-9968-7

Glocer, A., Kitamura, N., Toth, G., & Gombosi, T. (2012). Modeling solar zenith angle effects on the polar wind. *Journal of Geophysical Research*, *117*(A4), A04318. https://doi.org/10.1029/2011JA017136

Hasegawa, A., & Mima, K. (1978). Anomalous transport produced by kinetic Alfvén wave turbulence. *Journal of Geophysical Research*, *83*(A3), 1117. https://doi.org/10.1029/JA083iA03p01117

Hedin, A. E. (1991). Extension of the MSIS thermospheric model into the middle and lower atmosphere. *Journal of Geophysical Research*, *96*(A2), 1159–1172. https://doi.org/10.1029/90JA02125

Horne, R. B., & Thorne, R. M. (1998). Potential waves for relativistic electron scattering and stochastic acceleration during magnetic storms. *Geophysical Research Letters*, *25*(15), 3011–3014. https://doi.org/10.1029/98GL01002

Khazanov, G. V. (2010). Kinetic theory of inner magnetospheric plasma. In *Astrophysics and space science library* (Vol. 372, p. 584). Springer Science & Business Media.

Khazanov, G. V., Gamayunov, K. V., Gallagher, D. L., Kozyra, J. U., & Liemohn, M. W. (2007). Self-consistent model of magnetospheric ring current and propagating electromagnetic ion cyclotron waves: 2. Wave-induced ring current precipitation and thermal electron heating. *Journal of Geophysical Research*, *112*(A4), A04209. https://doi.org/10.1029/2006JA012033

Khazanov, G. V., Glocer, A., & Chu, M. (2020). The formation of electron heat flux in the region of diffuse aurora. *Journal of Geophysical Research: Space Physics*, *125*(8), e2020JA028175. https://doi.org/10.1029/2020JA028175

Khazanov, G. V., Glocer, A., & Chu, M. (2021). Electron energy interplay in the geomagnetic trap below the auroral acceleration region. *Journal of Geophysical Research: Space Physics*, *126*(5), e2020JA028811. https://doi.org/10.1029/2020JA028811

Khazanov, G. V., Glocer, A., & Himwich, E. W. (2014). Magnetosphere-ionosphere energy interchange in the electron diffuse aurora. *Journal of Geophysical Research: Space Physics*, *119*(1), 171–184. https://doi.org/10.1002/2013JA019325

Khazanov, G. V., Himwich, E. W., Glocer, A., & Sibeck, D. (2016). The role of multiple atmospheric reflections in the formation of th electron distribution function in the diffuse aurora region. *Auroral Dynamics and Space Weather, Geophysical Monograph Series*, *215*, 115–130. https://doi.org/10.1002/9781118978719

Khazanov, G. V., & Ma, Q. (2021). Dayside low energy electron precipitation driven by hiss waves in the presence of ionospheric photoelectrons. *Journal of Geophysical Research: Space Physics*, *126*(12), e2021JA030048. https://doi.org/10.1029/2021JA030048

Khazanov, G. V., Shen, Y., Vasko, I. Y., Artemyev, A. V., & Chu, M. (2021). Magnetosphere-ionosphere coupling of precipitated electrons in diffuse aurora driven by time domain structures. *Geophysical Research Letters*, *48*(10), e2021GL092655. https://doi.org/10.1029/2021GL092655

Khazanov, G. V., Sibeck, D. G., & Zesta, E. (2017). Major pathways to electron distribution function formation in regions of diffuse aurora. *Journal of Geophysical Research: Space Physics*, *122*(4), 4251–4265. https://doi.org/10.1002/2017JA023956

Khazanov, G. V., Sibeck, D. G., & Zesta, E. (2019). The formation of electron heat flux over the sunlit quiet polar cap ionosphere. *Geophysical Research Letters*, *46*(17–18), 10201–10208. https://doi.org/10.1029/2019GL084522

Khazanov, G. V., Tripathi, A. K., Singhal, R. P., Himwich, E. W., Glocer, A., & Sibeck, D. G. (2015). Superthermal electron magnetosphere-ionosphere coupling in the diffuse aurora in the presence of ECH waves. *Journal of Geophysical Research: Space Physics*, *120*(1), 445–459. https://doi.org/10.1002/2014JA020641

Kletzing, C. A., Kurth, W. S., Acuna, M., MacDowall, R. J., Torbert, R. B., Averkamp, T., et al. (2013). The electric and magnetic field instrument suit and integrated science (EMFISIS) on RBSP. *Space Science Reviews*, *179*(1–4), 127–181. https://doi.org/10.1007/s11214-013-9993-6

Kozyra, J. U., Shelley, E. G., Comfort, R. H., Brace, L. H., Cravens, T. E., & Nagy, A. F. (1987). The role of ring current O^+ in the formation of stable auroral red arcs. *Journal of Geophysical Research*, *92*(A7), 7487. https://doi.org/10.1029/JA092iA07p07487

Kurth, W. S., De Pascuale, S., Faden, J. B., Kletzing, C. A., Hospodarsky, G. B., Thaller, S., & Wygant, J. R. (2015). Electron densities inferred from plasma wave spectra obtained by the Waves instrument on Van Allen Probes. *Journal of Geophysical Research: Space Physics*, *120*(2), 904–914. https://doi.org/10.1002/2014JA020857

Li, J., Ma, Q., Bortnik, J., Li, W., An, X., Reeves, G. D., et al. (2019). Parallel acceleration of suprathermal electrons caused by whistler-mode hiss waves. *Geophysical Research Letters*, *46*(22), 12675–12684. https://doi.org/10.1029/2019GL085562

Li, W., Ma, Q., Thorne, R. M., Bortnik, J., Kletzing, C. A., Kurth, W. S., et al. (2015). Statistical properties of plasmaspheric hiss derived from Van Allen Probes data and their effects on radiation belt electron dynamics. *Journal of Geophysical Research: Space Physics*, *120*(5), 3393–3405. https://doi.org/10.1002/2015JA021048

Li, W., Santolik, O., Bortnik, J., Thorne, R. M., Kletzing, C. A., Kurth, W. S., & Hospodarsky, G. B. (2016). New chorus wave properties near the equator from Van Allen Probes wave observations. *Geophysical Research Letters*, *43*(10), 4725–4735. https://doi.org/10.1002/2016GL068780

Li, W., Shen, X.-C., Ma, Q., Capannolo, L., Shi, R., Redmon, R. J., et al. (2019). Quantification of energetic electron precipitation driven by plume whistler mode waves, plasmaspheric hiss, and exohiss. *Geophysical Research Letters*, *46*(7), 3615–3624. https://doi.org/10.1029/2019GL082095

Li, W., Thorne, R. M., Angelopoulos, V., Bortnik, J., Cully, C. M., Ni, B., et al. (2009). Global distribution of whistler-mode chorus waves observed on the THEMIS spacecraft. *Geophysical Research Letters*, *36*(9), L09104. https://doi.org/10.1029/2009GL037595

Li, W., Thorne, R. M., Bortnik, J., Reeves, G. D., Kletzing, C. A., Kurth, W. S., et al. (2013). An unusual enhancement of low-frequency plasmaspheric hiss in the outer plasmasphere associated with substorm-injected electrons. *Geophysical Research Letters*, *40*(15), 3798–3803. https://doi.org/10.1002/grl.50787

Li, W., Thorne, R. M., Nishimura, Y., Bortnik, J., Angelopoulos, V., McFadden, J. P., et al. (2010). THEMIS analysis of observed equatorial electron distributions responsible for the chorus excitation. *Journal of Geophysical Research*, *115*(A6), A00F11. https://doi.org/10.1029/2009JA014845

Lyons, L. R., & Thorne, R. M. (1973). Equilibrium structure of radiation belt electrons. *Journal of Geophysical Research*, *78*(13), 2142–2149. https://doi.org/10.1029/ja078i013p02142

Ma, Q., Artemyev, A. V., Mourenas, D., Li, W., Thorne, R. M., Kletzing, C. A., et al. (2017). Very oblique whistler mode propagation in the radiation belts: Effects of hot plasma and Landau damping. *Geophysical Research Letters*, *44*(24), 12057–12066. https://doi.org/10.1002/2017GL075892

Ma, Q., Connor, H. K., Zhang, X.-J., Li, W., Shen, X.-C., Gillespie, D., et al. (2020). Global survey of plasma sheet electron precipitation due to whistler mode chorus waves in Earth's magnetosphere. *Geophysical Research Letters*, *47*(15), e2020GL088798. https://doi.org/10.1029/2020GL088798

Ma, Q., Li, W., Thorne, R. M., & Angelopoulos, V. (2013). Global distribution of equatorial magnetosonic waves observed by THEMIS. *Geophysical Research Letters*, *40*(10), 1895–1901. https://doi.org/10.1002/grl.50434

Ma, Q., Li, W., Zhang, X.-J., Bortnik, J., Shen, X.-C., Connor, H. K., et al. (2021). Global survey of electron precipitation due to hiss waves in the Earth's plasmasphere and plumes. *Journal of Geophysical Research: Space Physics*, *126*(8), e2021JA029644. https://doi.org/10.1029/2021JA029644

Mauk, B. H., Fox, N. J., Kanekal, S. G., Kessel, R. L., Sibeck, D. G., & Ukhorskiy, A. (2013). Science objectives and rationale for the radiation belt storm probes mission. *Space Science Reviews*, *179*(1–4), 1–15. https://doi.org/10.1007/s11214-012-9908-y

McIntosh, R. C., & Anderson, P. C. (2014). Maps of precipitating electron spectra characterized by Maxwellian and kappa distributions. *Journal of Geophysical Research: Space Physics*, *119*, 10116–10132. https://doi.org/10.1002/2014JA02008

Meredith, N. P., Horne, R. B., Clilverd, M. A., Horsfall, D., Thorne, R. M., & Anderson, R. R. (2006). Origins of plasmaspheric hiss. *Journal of Geophysical Research*, *111*(A9), A09217. https://doi.org/10.1029/2006JA011707

Meredith, N. P., Horne, R. B., Glauert, S. A., & Anderson, R. R. (2007). Slot region electron loss timescales due to plasmaspheric hiss and lightning-generated whistlers. *Journal of Geophysical Research*, *112*(A8), A08214. https://doi.org/10.1029/2007JA012413

Meredith, N. P., Horne, R. B., Glauert, S. A., Thorne, R. M., Summers, D., Albert, J. M., & Anderson, R. R. (2006). Energetic outer zone electron loss timescales during low geomagnetic activity. *Journal of Geophysical Research*, *111*(A5), A05212. https://doi.org/10.1029/2005JA011516

Meredith, N. P., Horne, R. B., Kersten, T., Li, W., Bortnik, J., Sicard, A., & Yearby, K. H. (2018). Global model of plasmaspheric hiss from multiple satellite observations. *Journal of Geophysical Research: Space Physics*, *123*(6), 4526–4541. https://doi.org/10.1029/2018JA025226

Meredith, N. P., Horne, R. B., Li, W., Thorne, R. M., & Sicard-Piet, A. (2014). Global model of low-frequency chorus (f_{LHR}<f<0.1f_{ce}) from multiple satellite observations. *Geophysical Research Letters*, *41*(2), 280–286. https://doi.org/10.1002/2013GL059050

Meredith, N. P., Horne, R. B., Shen, X.-C., Li, W., & Bortnik, J. (2020). Global model of whistler mode chorus in the near-equatorial region (|λm|< 18°). *Geophysical Research Letters*, *47*(11), e2020GL087311. https://doi.org/10.1029/2020GL087311

Meredith, N. P., Horne, R. B., Sicard-Piet, A., Boscher, D., Yearby, K. H., Li, W., & Thorne, R. M. (2012). Global model of lower band and upper band chorus from multiple satellite observations. *Journal of Geophysical Research*, *117*(A10), A10225. https://doi.org/10.1029/2012JA017978

Mishin, E., & Streltsov, A. (2021). *Nonlinear wave and plasma structures in the auroral and subauroral geospace* (p. 621). Elsevier.

Mishin, E. V. (2019). Artificial aurora experiments and application to natural aurora. *Frontiers in Astronomy and Space Sciences*, *6*, 14. https://doi.org/10.3389/fspas.2019.00014

Ni, B., Bortnik, J., Thorne, R. M., Ma, Q., & Chen, L. (2013). Resonant scattering and resultant pitch angle evolution of relativistic electrons by plasmaspheric hiss. *Journal of Geophysical Research: Space Physics*, *118*(12), 7740–7751. https://doi.org/10.1002/2013JA019260

Ni, B., Li, W., Thorne, R. M., Bortnik, J., Ma, Q., Chen, L., et al. (2014). Resonant scattering of energetic electrons by unusual low-frequency hiss. *Geophysical Research Letters*, *41*(6), 1854–1861. https://doi.org/10.1002/2014GL059389

Ni, B., Thorne, R. M., Meredith, N. P., Horne, R. B., & Shprits, Y. Y. (2011). Resonant scattering of plasma sheet electrons leading to diffuse auroral precipitation: 2. Evaluation for whistler mode chorus waves. *Journal of Geophysical Research*, *116*(A4), A04219. https://doi.org/10.1029/2010JA016233

Richmond, A. D., Ridley, E. C., & Roble, R. G. (1992). A thermosphere/ionosphere general circulation model with coupled electrodynamics. *Geophysical Research Letters*, *19*(6), 601–604. https://doi.org/10.1029/92gl00401

Ridley, A. J., Deng, Y., & Toth, G. (2006). The global ionosphere–thermosphere model. *Journal of Atmospheric and Solar-Terrestrial Physics*, *68*(8), 839–864. https://doi.org/10.1016/j.jastp.2006.01.008

Samara, M., Michell, R. G., & Khazanov, G. V. (2017). First optical observations of interhemispheric electron reflections within pulsating aurora. *Geophysical Research Letters*, *44*, 2618–2623. https://doi.org/10.1002/2017GL072794

Schunk, R. W., & Nagy, A. F. (2009). *Ionospheres: Physics, plasma physics, and chemistry*. Cambridge University Press.

Schunk, R. W., Sojka, J. J., & Bowline, M. D. (1986). Theoretical study of the electron temperature in the high-latitude ionosphere for solar maximum and winter conditions. *Journal of Geophysical Research*, *91*(A11), 12041–12054. https://doi.org/10.1029/JA091iA11p12041

Scudder, J. D., Cao, X., & Mozer, F. S. (2000). Photoemission current-spacecraft voltage relation: Key to routine, quantitative low-energy plasma measurements. *Journal of Geophysical Research*, *105*(A9), 21281–21294. https://doi.org/10.1029/1999JA900423

Sheeley, B. W., Moldwin, M. B., Rassoul, H. K., & Anderson, R. R. (2001). An empirical plasmasphere and trough density model: CRRES observations. *Journal of Geophysical Research*, *106*(A11), 25631–25641. https://doi.org/10.1029/2000JA000286

Shi, R., Li, W., Ma, Q., Green, A., Kletzing, C. A., Kurth, W. S., et al. (2019). Properties of whistler mode waves in Earth's plasmasphere and plumes. *Journal of Geophysical Research: Space Physics*, *124*(2), 1035–1051. https://doi.org/10.1029/2018JA026041

Solomon, S., Hays, P., & Abreu, V. (1988). The auroral 6300. emission: Observations and modeling. *Journal of Geophysical Research*, *93*(A9), 9867–9882. https://doi.org/10.1029/JA093iA09p09867

Sonwalkar, V. S., & Inan, U. S. (1989). Lightning as an embryonic source of VLF hiss. *Journal of Geophysical Research*, *94*(A6), 6986–6994. https://doi.org/10.1029/JA094iA06p06986

Spence, H. E., Reeves, G. D., Baker, D. N., Blake, J. B., Bolton, M., Bourdarie, S., et al. (2013). Science goals and overview of the radiation belt storm probes (RBSP) energetic particle, composition, and thermal plasma (ECT) suite on NASA's Van Allen probes mission. *Space Science Reviews*, *179*(1–4), 311–336. https://doi.org/10.1007/s11214-013-0007-5

Thorne, R. M. (2010). Radiation belt dynamics: The importance of wave-particle interactions. *Geophysical Research Letters*, *37*(22), L22107. https://doi.org/10.1029/2010GL044990

Thorne, R. M., Bortnik, J., Li, W., & Ma, Q. (2021). Wave–particle interactions in the Earth's magnetosphere. In R. Maggiolo, N. André, H. Hasegawa, D. T. Welling, Y. Zhang, & L. J. Paxton (Eds.), *Magnetospheres in the solar system*. https://doi.org/10.1002/9781119815624.ch6

Thorne, R. M., Li, W., Ni, B., Ma, Q., Bortnik, J., Baker, D. N., et al. (2013). Evolution and slow decay of an unusual narrow ring of relativistic electrons near $L \sim 3.2$ following the September 2012 magnetic storm. *Geophysical Research Letters*, *40*(14), 3507–3511. https://doi.org/10.1002/grl.50627

Thorne, R. M., Ni, B., Tao, X., Horne, R. B., & Meredith, N. P. (2010). Scattering by chorus waves as the dominant cause of diffuse auroral precipitation. *Nature*, *467*(7318), 943–946. https://doi.org/10.1038/nature09467